Supporting Information for Overcoming Barriers to Dynamic Phase-only Modulation in Transmissive Metasurfaces via Diffraction Control

Juyoung Kim†, Ruzan Sokhoyan†, Minkyoon Yi, Sangjun Han, Harry Atwater*, Min Seok Jang*

1 Temporal Coupled-Mode Theory

The model framework that we utilize to analyze and design the system is the temporal coupled-mode theory (TCMT) [1]. The validity of TCMT is described in detail in [2]. The dynamics of amplitude a of a resonance mode (We will only deal with single-resonance systems in this paper) can be described by the following equations:

$$\frac{da}{dt} = -i\tilde{\omega}_0 a + \langle \kappa^* | s_+ \rangle \tag{S1}$$

$$|s_-\rangle = C|s_+\rangle + a|d\rangle \tag{S2}$$

where $\tilde{\omega}_0 = \omega_0 + i\gamma$ is the complex resonance frequency whose real (ω_0) and imaginary (γ) parts are the center frequency and the overall decay rate of the resonance, respectively. Here $|a|^2$ is normalized to be the energy of the corresponding mode, $|s_+\rangle$ and $|s_-\rangle$ are the vectors of amplitudes of the incoming and outgoing waves, and their number of elements is equal to the number of input (m_+) and output (m_-) ports, respectively. $|d\rangle$ and $|d\rangle$ are m_+ and m_- dimensional vectors describing the coupling from the input port to the resonance, and from the resonance to the output port, respectively. C is the $m_- \times m_+$ direct scattering matrix from input to output ports. Note that there is freedom in choosing where the ports are placed from the resonator, which allows the complex parameters in the terms $|d\rangle$, $|\kappa\rangle$ and C to be decided up to a factor $e^{ikl} = e^{i\theta}$, where l is the port's distance from the resonator. This allows us to later adopt the convention used in the main paper, which is to place all the ports such that the coupling parameters $|d\rangle$ take on real values. This convention is possible for single-resonance systems, but is not guaranteed for systems with multiple resonances as choosing the set of port distances that gives real coupling parameters for one resonance does not generally make the coupling parameters real for the other resonances. Also, choosing the coupling parameters $|d\rangle$ to be real simultaneously affects the complex parameters of the direct scattering matrix C, and generally results in complex values for C.

For generality, we will start off with a four-port system and reduce to two-port systems when necessary. There can be many ways to make the system have four ports - by using different polarizations, nonzero incidence angles, or diffraction orders. We will assume to have two additional diffraction ports, but the mathematics for systems with more diffraction ports (such as the six-port system in the main paper) is similar. Imagine a four-port system as follows (Fig. S1):

Notice that no assumptions on 'where' the ports 1, 2, 3, 4 are positioned are used in the following derivations, only the fact that port 3 = port 4 due to symmetry. The figure below is just for illustrative purposes. The analysis below is more general than what's shown in the figure, as the following formalism can also take into account systems with ports 3 and 4 on port 2's side, and systems with ports 1 and 2 'misaligned' or at an angle with one another, and many other configurations.

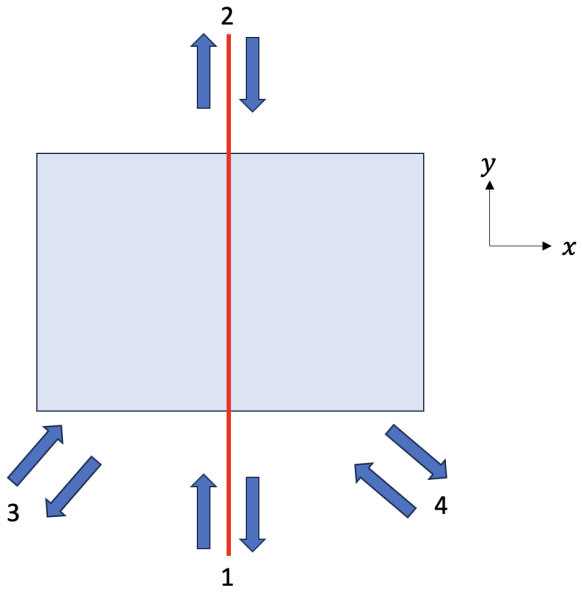


Figure S1: A four-port system with parity symmetry in the x-direction across the y-axis

Then along with Eq. S1 and S2 above, we have for the incoming and outgoing wave vectors and the coupling vectors:

$$|s_-\rangle = \begin{pmatrix} s_{1-} \\ s_{2-} \\ s_{3-} \\ s_{4-} \end{pmatrix} \quad |s_+\rangle = \begin{pmatrix} s_{1+} \\ s_{2+} \\ s_{3+} \\ s_{4+} \end{pmatrix} \quad |\kappa\rangle = \begin{pmatrix} \kappa_1 \\ \kappa_2 \\ \kappa_3 \\ \kappa_4 \end{pmatrix} \quad |d\rangle = \begin{pmatrix} d_1 \\ d_2 \\ d_3 \\ d_4 \end{pmatrix}$$

and the direct scattering matrix C is given by:

$$C = \begin{pmatrix} c_{11} & c_{12} & c_{13} & c_{14} \\ c_{21} & c_{22} & c_{23} & c_{24} \\ c_{31} & c_{32} & c_{33} & c_{34} \\ c_{41} & c_{42} & c_{43} & c_{44} \end{pmatrix}$$

where c_{ij} refers to the direct scattering term from port i to port j.

Applying time reversal symmetry, energy conservation, and reciprocity [1] we get

$$\langle d|d\rangle = \frac{2}{\tau} \tag{S3}$$

$$|d\rangle = |\kappa\rangle \tag{S4}$$

$$C|d\rangle^* = -|d\rangle \tag{S5}$$

Also, assuming parity symmetry in the x-direction about the y-axis as shown in Fig. S1 above, and also assuming that the resonance field profile in question is also even about the y-axis (our mode belongs to this class), as well as applying time reversal symmetry, energy conservation, and reciprocity ([3]) we get the following scattering matrix C :

$$C = \begin{pmatrix} r_1 & t & \alpha & \alpha \\ t & r_2 & \beta & \beta \\ \alpha & \beta & c & e \\ \alpha & \beta & e & c \end{pmatrix}$$

with the following norm equations:

$$|r_1|^2 + |t|^2 + 2|\alpha|^2 = 1 \tag{S6}$$

$$|t|^2 + |r_2|^2 + 2|\beta|^2 = 1 \tag{S7}$$

$$|\alpha|^2 + |\beta|^2 + |c|^2 + |e|^2 = 1 \tag{S8}$$

and the following orthogonality relations:

$$r_1 t^* + t r_2{}^* + 2\alpha\beta^* = 0 \tag{S9}$$

$$r_1\alpha^* + t\beta^* + \alpha c^* + \alpha e^* = 0 \tag{S10}$$

$$t\alpha^* + r_2\beta^* + \beta c^* + \beta e^* = 0 \tag{S11}$$

$$|\alpha|^2 + |\beta|^2 + ce^* + ec^* = 0 \tag{S12}$$

By assuming steady state excitation we have:

$$a = \frac{\langle \kappa^* | s_+ \rangle}{-i(\omega - \omega_0) + \gamma} \tag{S13}$$

where $\gamma = \frac{1}{\tau} = \gamma_1 + \gamma_2 + \gamma_3 + \gamma_4 + \gamma_d$. Here γ_i refers to the radiative coupling amplitudes (energy loss) for each port, and γ_d refers to dissipative loss. The radiative coupling d_i, which is tied to the decay/gain in the field amplitude of the resonance (rather than the energy of the resonance, like the γ_i terms) is related to the γ_i terms through Eq.S1 above, and by turning 'on' only a single port while the other ports are turned 'off'. This gives rise to $d_i = \sqrt{2\gamma_i} e^{i\theta_i}$.

Now to get the relation between the coupling coefficients d_i and the direct scattering coefficients of matrix C, we use Eq.S3 above:

$$\begin{pmatrix} r_1 & t & \alpha & \alpha \\ t & r_2 & \beta & \beta \\ \alpha & \beta & c & e \\ \alpha & \beta & e & c \end{pmatrix} \begin{pmatrix} d_1^* \\ d_2^* \\ d_3^* \\ d_4^* \end{pmatrix} = - \begin{pmatrix} d_1 \\ d_2 \\ d_3 \\ d_4 \end{pmatrix}$$

Then we get:

$$r_1 d_1^* + t d_2^* + \alpha(d_3^* + d_4^*) = -d_1 \tag{S14}$$

$$t d_1^* + r_2 d_2^* + \beta(d_3^* + d_4^*) = -d_2 \tag{S15}$$

$$\alpha d_1^* + \beta d_2^* + c d_3^* + e d_4^* = -d_3 \tag{S16}$$

$$\alpha d_1^* + \beta d_2^* + e d_3^* + c d_4^* = -d_4 \tag{S17}$$

Although due to symmetry and the even field profile we have $d_3 = d_4$, we will still denote them as d_3 and d_4 separately.

Now applying $|s_-\rangle = C|s_+\rangle + a|d\rangle$:

$$\begin{pmatrix} s_{1-} \\ s_{2-} \\ s_{3-} \\ s_{4-} \end{pmatrix} = \begin{pmatrix} r_1 & t & \alpha & \alpha \\ t & r_2 & \beta & \beta \\ \alpha & \beta & c & e \\ \alpha & \beta & e & c \end{pmatrix} \begin{pmatrix} s_{1+} \\ s_{2+} \\ s_{3+} \\ s_{4+} \end{pmatrix} + a \begin{pmatrix} d_1 \\ d_2 \\ d_3 \\ d_4 \end{pmatrix}$$

Because the incident light is only coming through port 1, $s_{2+} = s_{3+} = s_{4+} = 0$ and along with Eq.S13

$$\mathbf{r} = \frac{s_{1-}}{s_{1+}} = r_1 + \frac{i d_1^2}{(\omega - \omega_0) + i\gamma} = r_1 + \frac{2i\gamma_1 e^{2i\theta_1}}{(\omega - \omega_0) + i\gamma} \equiv \mathbf{A_r} + \mathbf{B_r} \tag{S18}$$

$$\mathbf{t} = \frac{s_{2-}}{s_{1+}} = t + \frac{i d_1 d_2}{(\omega - \omega_0) + i\gamma} = t + \frac{2i\sqrt{\gamma_1 \gamma_2} e^{i(\theta_1 + \theta_2)}}{(\omega - \omega_0) + i\gamma} \equiv \mathbf{A_t} + \mathbf{B_t} \tag{S19}$$

$$\mathbf{r_{10}} = \frac{s_{3-}}{s_{1+}} = \alpha + \frac{id_1d_3}{(\omega-\omega_0)+i\gamma} = \alpha + \frac{2i\sqrt{\gamma_1\gamma_3}e^{i(\theta_1+\theta_3)}}{(\omega-\omega_0)+i\gamma} \equiv \mathbf{A_{d1}} + \mathbf{B_{d1}}$$

Now we are in the position to examine how the $\mathbf{A_{t,r}}$ and $\mathbf{B_{t,r}}$ behave. Let's look at them one by one:

First, they were denoted in bold because on the complex plane, if you think of their real parts as the x-axis projections and their imaginary parts as the y-axis projections, we can think of them as 2-D vectors.

Second, the terms $\mathbf{A_{t,r}}$ are relatively constant as the changes in $\omega - \omega_0$ make a significant difference in the overall transmission and reflection curves, provided that the losses γ_d in γ don't render the 'widths' (FWHM in the case of a Lorentzian curve) of these curves to be too large (in which case the curves will likely be useless for phase modulation, which we shall soon see).

Third, the terms $\mathbf{B_{t,r}}$ draw a circle on the complex plane as the ω sweeps from 0 to ∞. We can see this as follows. Let's first isolate the common term from $\mathbf{B_{t,r}}$ and rewrite it by making the denominator real:

$$\frac{i}{(\omega-\omega_0)+i\gamma} = \frac{i}{\sqrt{(\omega-\omega_0)^2+\gamma^2}}e^{i\alpha}$$

where the term α was defined so that $\cos\alpha = \frac{\omega-\omega_0}{\sqrt{(\omega-\omega_0)^2+\gamma^2}}$ and $\sin\alpha = \frac{-\gamma}{\sqrt{(\omega-\omega_0)^2+\gamma^2}}$. Denoting $\omega - \omega_0 = \overline{\omega}$ for simplicity, we can see that as ω goes from 0 to ∞, $\overline{\omega}$ goes as roughly $-\infty \to \infty$ (ω_0 is a very large number typically). Then from the definition of the $\cos\alpha$, it goes as $-1 \to 1$, and coupled with that fact that $\sin\alpha$ is negative due to $-\gamma < 0$ ($\alpha < 0$), we can see that α sweeps as $-\pi \to 0$ from the reference of i (the imaginary axis). We can see this in Fig. S2 below.

Now, to see that the common term in $\mathbf{B_{t,r}}$ terms draw out a circle, we write it as:

$$\frac{-\sin\alpha}{\sqrt{(\omega-\omega_0)^2+\gamma^2}} + i\frac{\cos\alpha}{\sqrt{(\omega-\omega_0)^2+\gamma^2}} = \frac{\gamma}{(\omega-\omega_0)^2+\gamma^2} + i\frac{\omega-\omega_0}{(\omega-\omega_0)^2+\gamma^2} \equiv x + iy$$

Now, showing that x and y satisfy the equation of a circle:

$$x^2 + y^2 = \frac{\gamma^2}{((\omega-\omega_0)^2+\gamma^2)^2} + \frac{(\omega-\omega_0)^2}{((\omega-\omega_0)^2+\gamma^2)^2} = \frac{(\omega-\omega_0)^2+\gamma^2}{((\omega-\omega_0)^2+\gamma^2)^2} = \frac{1}{(\omega-\omega_0)^2+\gamma^2}$$

$$x^2 - \frac{1}{(\omega-\omega_0)^2+\gamma^2} + y^2 + \frac{1}{(2\gamma)^2} = \frac{1}{(2\gamma)^2}$$

$$x^2 - 2(\frac{\gamma}{(\omega-\omega_0)^2+\gamma^2})(\frac{1}{2\gamma}) + y^2 + \frac{1}{(2\gamma)^2} = \frac{1}{(2\gamma)^2}$$

Defining $R' = \frac{1}{2\gamma}$ we can see the equation becomes:

$$(x-R')^2 + y^2 = R'^2$$

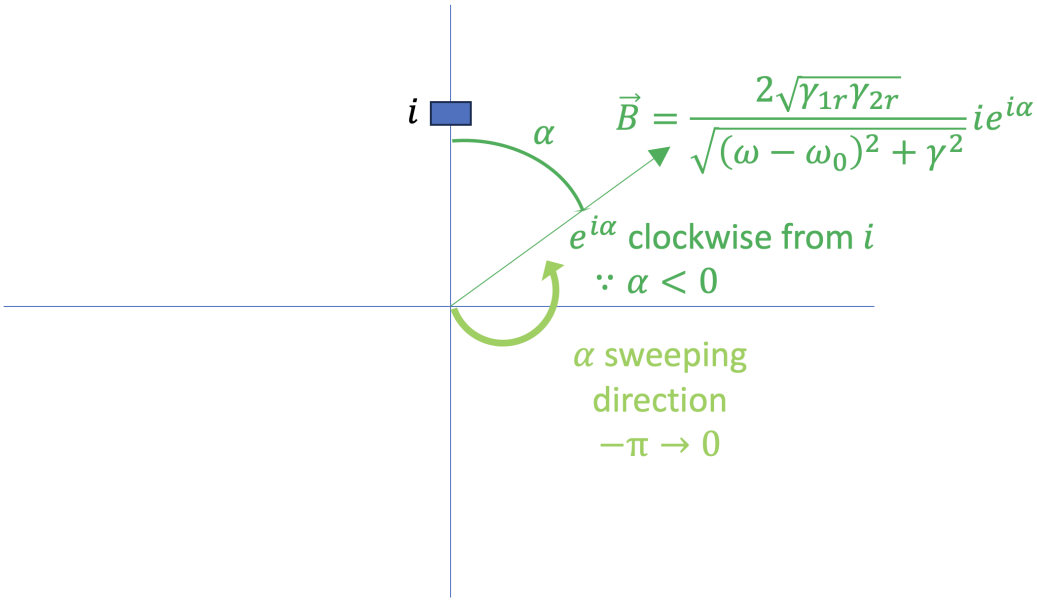


Figure S2: The sweeping of the B vector in the right side plane

This shows that the common term in $\mathbf{B_{t,r}}$ satisfies the equation of a circle defined on the complex plane, with the radius of R' and the center $(R', 0)$. Then, with the corresponding factors on either $\mathbf{B_{t,r}}$, we can see that $\mathbf{B_{t,r}}$ draws out a circle like below in Fig. S3, with $\mathbf{B_t}$ having $R = \frac{\sqrt{\gamma_1\gamma_2}}{\gamma}$ and $\Theta = \theta_1 + \theta_2$, while $\mathbf{B_r}$ has $R = \frac{\gamma_1}{\gamma}$ and $\Theta = 2\theta_1$.

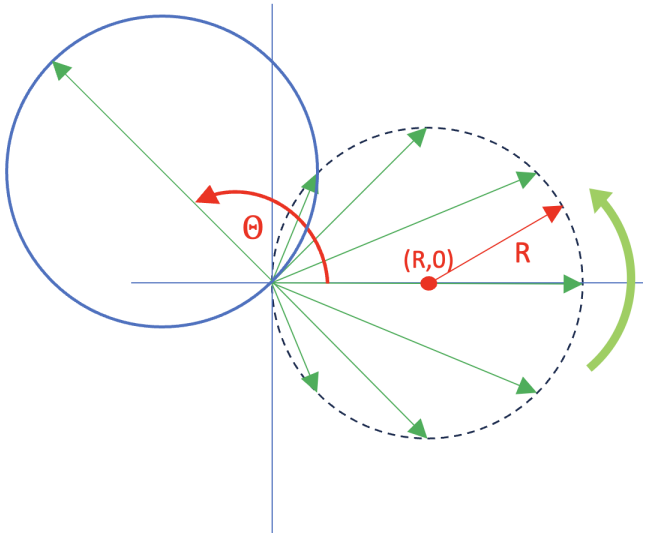


Figure S3: The $B_{t,r}$ vector drawing a circle on the complex plane

Now, before we see whether or not the transmission amplitude circle encircles around the origin on the complex plane, let's first rotate the complex transmission amplitude circle by $-\Theta = -(\theta_1 + \theta_2)$.

Then we have:

$$\mathbf{t}e^{-i(\theta_1+\theta_2)} = te^{-i(\theta_1+\theta_2)} + \frac{2i\sqrt{\gamma_1\gamma_2}}{(\omega-\omega_0)+i\gamma} \equiv \mathbf{A}+\mathbf{B} \tag{S20}$$

The reason for this is two-fold. One, we will now adopt the convention assumed in the main paper ($\theta_1 = \theta_2 = 0$, the real coupling condition), which, from the above, allows us to adopt the framework of displacing the term $\frac{2i\sqrt{\gamma_1\gamma_2}}{(\omega-\omega_0)+i\gamma}$ by the 'direct scattering parameter' $t_d = te^{-i(\theta_1+\theta_2)}$ in the main paper, and two, this illustrates the point made in the paper that changes in the radiative coupling values will naturally change θ_i and therefore will be reflected as 'compensated' changes in $\arg[t_{d,\mathbf{Im}[d_i]=0-convention}] = \arg[te^{-i(\theta_1+\theta_2)}]$.

Let's now adopt the real coupling condition where the $\theta_i = 0$, by placing the ports accordingly. Then we can observe that the circle is displaced by the t vector, but its angular orientation is maintained, with the $t = \mathbf{A}$ vector being the circle's leftmost point and the rightmost point corresponding to the resonance frequency $\omega = \omega_0$ (the latter fact can be quickly checked by seeing that putting in $\omega = \omega_0$ in $\mathbf{B}$ gives $\mathbf{B} = \frac{2\sqrt{\gamma_1\gamma_2}}{\gamma}$, which is purely positively real). Fig.S4 nicely illustrates this.

Now, back to the matter of the encircling of the origin. Graphically, this can result in 3 scenarios: The transmission circle NOT encircling the origin (Fig. S4a), encircling the origin (Fig. S4b), and exactly going through the origin (Fig. S3). The mathematical determinant for the encirclement of the origin is given by $R^2 - |\mathbf{C}|^2$ and its sign, where $\mathbf{C}$ is the displacement vector of the center of the circle from the origin, and is given by $\mathbf{C} = \mathbf{A} + \frac{\sqrt{\gamma_1\gamma_2}}{\gamma} = (\frac{\sqrt{\gamma_1\gamma_2}}{\gamma} + \mathbf{Re}[t]) + i(\mathbf{Im}[t])$.

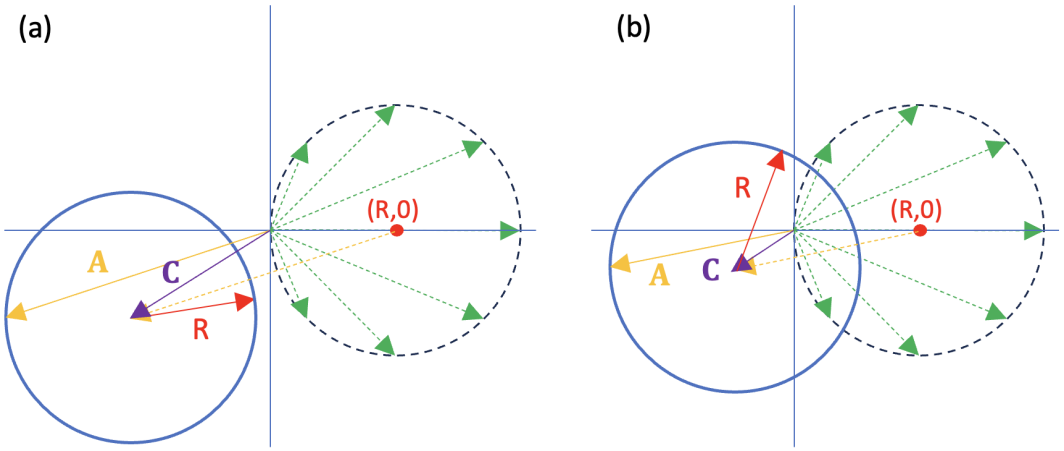


Figure S4: (a). The transmission circle not encircling the origin (b). The transmission circle encircling the origin

Now evaluating $R^2 - |\mathbf{C}|^2$ gives us

$$R^2 - |\mathbf{C}|^2 = (\frac{\sqrt{\gamma_1\gamma_2}}{\gamma})^2 - [(\frac{\sqrt{\gamma_1\gamma_2}}{\gamma} + \mathbf{Re}[t])^2 + (\mathbf{Im}[t])^2]$$

$$= (\frac{\sqrt{\gamma_1\gamma_2}}{\gamma})^2 - [(\frac{\sqrt{\gamma_1\gamma_2}}{\gamma})^2 + 2\frac{\sqrt{\gamma_1\gamma_2}}{\gamma}\mathbf{Re}[t] + (\mathbf{Re}[t])^2 + (\mathbf{Im}[t])^2]$$

$$= -2\frac{\sqrt{\gamma_1\gamma_2}}{\gamma}\mathbf{Re}[t] - |t|^2 \tag{S21}$$

Then rearranging Eq. S14 above and absolute-squaring it (now all the d_i terms are purely real), we have:

$$|r_1 + \alpha\frac{d_3+d_4}{d_1}|^2 = |-t\frac{d_2}{d_1} - 1|^2 = |t\sqrt{\frac{\gamma_2}{\gamma_1}} + 1|^2$$

$$= 1 + \frac{\gamma_2}{\gamma_1}|t|^2 + 2\sqrt{\frac{\gamma_2}{\gamma_1}}\mathbf{Re}[t]$$

Then we have the following from above:

$$-2\frac{\sqrt{\gamma_1\gamma_2}}{\gamma}\mathbf{Re}[t] = \frac{\gamma_1}{\gamma}(1 + \frac{\gamma_2}{\gamma_1}|t|^2 - |r_1 + \alpha\frac{\sqrt{2\gamma_3}+\sqrt{2\gamma_4}}{\sqrt{2\gamma_1}}|^2) \tag{S22}$$

Then inserting this into Eq. S21 above:

$$R^2 - |\mathbf{C}|^2 = \frac{\gamma_1}{\gamma}(1 + \frac{\gamma_2}{\gamma_1}|t|^2 - |r_1 + \alpha\frac{\sqrt{\gamma_3}+\sqrt{\gamma_4}}{\sqrt{\gamma_1}}|^2) - |t|^2$$

$$= \frac{\gamma_1}{\gamma}(1 - \frac{\gamma_1+\gamma_3+\gamma_4+\gamma_d}{\gamma_1}|t|^2 - |r_1 + \alpha\frac{\sqrt{\gamma_3}+\sqrt{\gamma_4}}{\sqrt{\gamma_1}}|^2) \tag{S23}$$

where we have used the fact that $\gamma = \gamma_1 + \gamma_2 + \gamma_3 + \gamma_4 + \gamma_d$.

Now in a two-port system, we have $\gamma_3 = \gamma_4 = \alpha = 0$ and $|t|^2 + |r_1|^2 = 1$ so we get:

$$R^2 - |\mathbf{C}|^2 = \frac{\gamma_1}{\gamma}(1 - \frac{\gamma_1+\gamma_d}{\gamma_1}|t|^2 - |r_1|^2) = -\frac{\gamma_d}{\gamma}|t|^2 < 0 \tag{S24}$$

Equation S24 shows that in a two-port system, as long as there are dissipative losses $\gamma_d > 0$ you will always have a complex transmission circle that doesn't encircle the origin (shown in Fig. 1 of the main paper, with the best case having the circle go through the origin when $\gamma_d = 0$. This means for a two-port system, unless you add gain to the system ($\gamma_d < 0$), the phase variation around the resonance will always be limited as $< 180°$. Also, from Eq. S21 and from the fact that $R^2 - |\mathbf{C}|^2 = -2\frac{\sqrt{\gamma_1\gamma_2}}{\gamma}\mathbf{Re}[t] - |t|^2 = 0$ when $\gamma_d = 0$, it follows that $\mathbf{Re}[t] < 0$

Now the idea behind using additional diffraction ports is this: Because $R^2 - |\mathbf{C}|^2 = 2\frac{\sqrt{\gamma_1\gamma_2}}{\gamma}|\mathbf{Re}[t]| - |t|^2 = 0$ just before diffraction is added (two-port system), if we can decrease the magnitude of $|t|$ through the additional terms in the energy conservation equation $|r_1|^2 + |t|^2 + 2|\alpha|^2 = 1$ and engineer the complex valued t so that $\mathbf{Re}[t] \approx t$, then we could have the second negative term $-|t|^2$ being smaller than the first positive term $2\frac{\sqrt{\gamma_1\gamma_2}}{\gamma}|\mathbf{Re}[t]|$ and have $R^2 - |\mathbf{C}|^2 > 0$.

Since we show that adding diffraction channels can indeed make $R^2 - |\mathbf{C}|^2 > 0$ in Fig. 2 of the main paper, we will now outline our objectives for optimal phase-only modulation.

1. We want the largest possible complex transmission amplitude circle, aka. having the largest radius $R = \frac{\sqrt{\gamma_1\gamma_2}}{\gamma_1+\gamma_2+\gamma_3+\gamma_4+\gamma_d}$

2. We want the circle centered as close to the origin as possible, aka. having the smallest $|\mathbf{C}| = |(\frac{\sqrt{\gamma_1\gamma_2}}{\gamma} + \mathbf{Re}[t]) + i(\mathbf{Im}[t])|$

We will now show below the conditions for having the largest possible radius while having $|\mathbf{C}| = 0$, making it a perfect phase-only modulation scheme.

First, the largest R is achieved when $\gamma_3 = \gamma_4 = \gamma_d = 0$ (restricting ourselves to the case of having no gain, $\gamma_d = 0$) and having $\gamma_1 = \gamma_2$, resulting in $R_{max} = 0.5$ (from the inequality $x + y \geq 2\sqrt{xy}$, with the equality holding when $x = y$). This makes sense intuitively, as we would expect the resonator spitting out equal number of photons per second into ports 1 and 2. While it is tempting to think that having $\gamma_2 > \gamma_1$ would be better, this would simply mean that not enough photons would come in through port 1 in the first place for port 2 to spit out (having a CAPACITY for port 2 to spit out 100 photons per second is meaningless if port 1 can ONLY take in 10 photons per second into the resonator).
Now, with that in mind, let's look at the condition of having $|\mathbf{C}| = 0$. This means having the following two conditions:

$$\mathbf{Re}[\mathbf{C}] = 0 \quad \rightarrow \quad \frac{\sqrt{\gamma_1\gamma_2}}{\gamma} = -\mathbf{Re}[t] \tag{S25}$$

$$\mathbf{Im}[\mathbf{C}] = 0 \quad \rightarrow \quad \mathbf{Im}[t] = 0 \tag{S26}$$

Because all the $\gamma's$ are defined to be positive, we can see from Eq. S25 that $\mathbf{Re}[t] < 0$, and from Eq. S26, we have the required condition that t is negative and real. Secondly, because $\frac{\sqrt{\gamma_1\gamma_2}}{\gamma}$ is the radius of the complex transmission amplitude circle, and our theoretical upper bound for the radius is 0.5, we can succinctly reduce the optimal conditions for transmissive phase-only modulation to be:

$$\arg[t] = \pi \tag{S27}$$

$$|t| = R = \frac{\sqrt{\gamma_1\gamma_2}}{\gamma} = 0.5 \tag{S28}$$

These are equations 2 and 3 in the main paper, and with these conditions the transmission circle starts at the baseline of $|t| = \frac{1}{2}$ from the negative real axis and draws a perfectly centered circle at the origin while maintaining the amplitude (radius) of 0.5.

We also add here, for the sake of completeness, the complex reflection amplitude circle akin to the complex transmission circles in Fig. 1 of the manuscript.

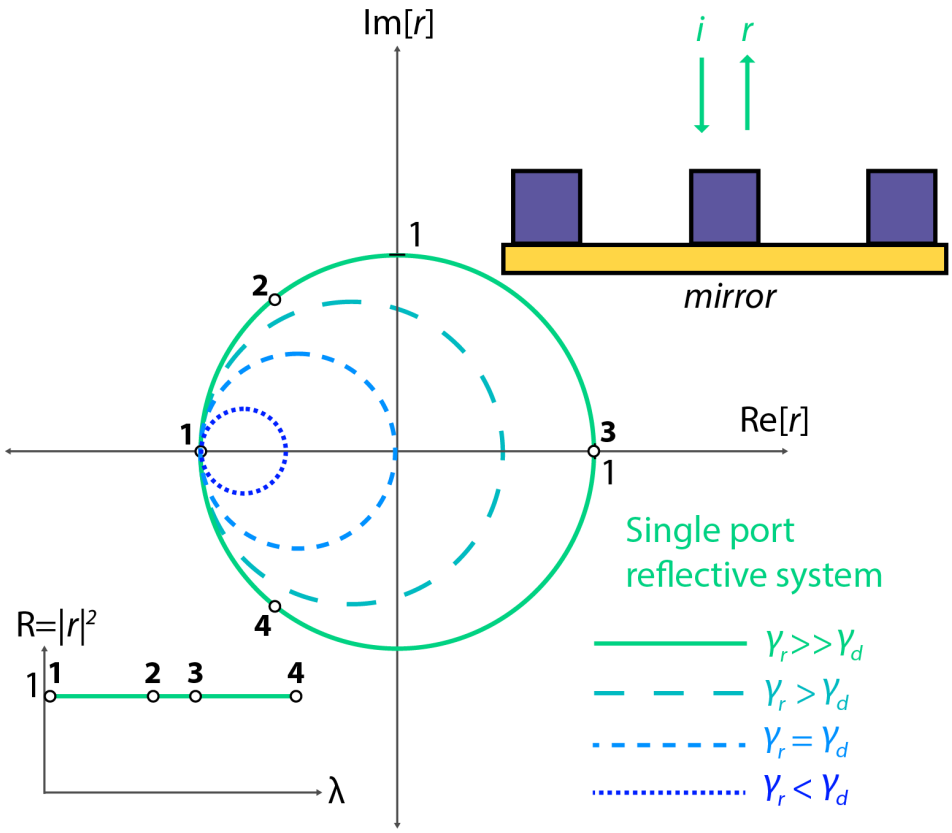


Figure S5: The complex reflection amplitude circles according to TCMT, with differing radiative and dissipative loss ratios

2 Figure 2 Details

The figures S5, S6, S7 below show the spectral transmittance and phase line plots for three periods ($P_x = 1344$ nm, $P_x = 1401.2$ nm, and $P_x = 1751.5$ nm), as well as the spectral reflection/diffraction plots for the diffraction-regime periods $P_x = 1401.2$ nm and $P_x = 1751.5$ nm in Fig. S7 and S8, respectively. R_{00} refers to normal reflection, and R_{10} refers to first-order diffraction in the $x-$direction.

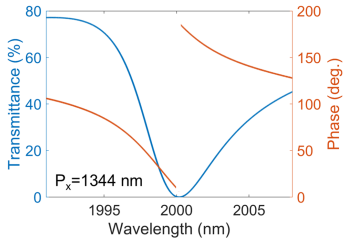


Figure S6: Transmittance and phase spectra for the metasurface depicted in Fig. 2 of the main manuscript. The period $P_x = 1344$ nm is smaller than the effective wavelength within the substrate (2000 nm/1.44 = 1388.9 nm). Hence, no diffraction is observed in reflection or transmission. Note that the phase exhibits discontinuity and spans 180 degrees.

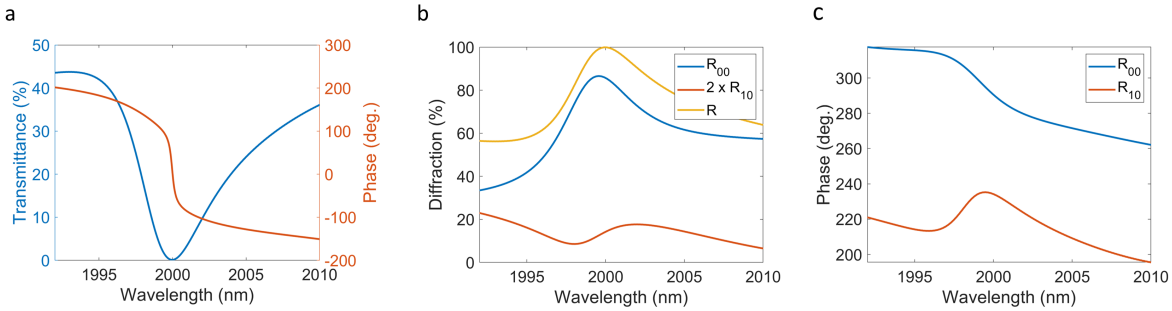


Figure S7: Transmittance and phase spectra for the metasurface with $P_x = 1401.2$ nm. The effective wavelength within the substrate is smaller than the metasurface period in the x-direction, and diffraction within the substrate is observed. (b) shows diffraction efficiencies in the normal direction R_{00} and in the x-direction R_{10}. Note that we plot $2 \times R_{10}$ to account for $\pm 1^{\text{st}}$ diffraction orders. (c) plots the phases of each of the diffracted waves.

In our work, as an illustrative example, we investigate a metasurface such that a metasurface element supports a 32-pole, or a "dotriacontapole" mode. The dotriacontapole mode is a spherical-tensor multipole of order $l = 5$, coming after the monopole ($l = 0$), dipole ($l = 1$), quadrupole ($l = 2$), octupole ($l = 3$), and hexadecapole ($l = 4$). Although our resonator geometry does not exhibit spherical symmetry, it is common practice to name modes in non-spherical systems according to their corresponding counterparts in spherical systems, since radiated fields can still be decomposed into multipolar components (for example, we use the term "electric dipole" in rectangular or cylindrical systems, even though dipoles are strictly spherical tensors).

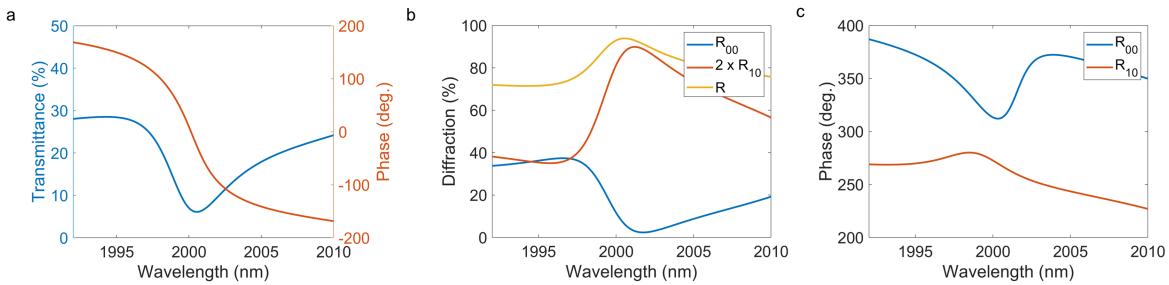


Figure S8: Transmittance and phase spectra for the metasurface with $P_x = 1751.5$ nm. The effective wavelength within the substrate is smaller than the metasurface period in the x-direction, and diffraction within the substrate is observed. (b) shows diffraction efficiencies in the normal direction R_{00} and in the x-direction R_{10}. Note that we plot $2 \times R_{10}$ to account for $\pm 1^{\text{st}}$ diffraction orders. (c) plots the phases of each of the diffracted waves.

Multipoles have various spatial configurations depending on the m value in the spherical harmonics Y_{lm}. For illustration, the hydrogen orbitals (which are also spherical tensors) provide a useful analogy. For example, the hydrogen orbitals f_{xz^2} or f_{yz^2} corresponding to $m = \pm 1$ in Y_{lm} exhibit a planar nature in their spatial field profiles, in contrast to the orbital f_{z^3}, which is linear, or f_{xyz}, which is three-dimensional. The planar-configuration quadrupoles have two electric field lobes on each side, octupoles have three on each, hexadecapoles have four on each, and dotriacontapoles have five on each side (see, for example, Jeon, J. and Lee, S., *Unveiling multipole physics and frustration of icosahedral magnetic quasicrystals*, *npj Quantum Mater.* **9**, 5 (2024), https://doi.org/10.1038/s41535-023-00617-z).

As the inset of Fig. 2b in our manuscript demonstrates, the field profile of our resonance shows five electric field lobes on both the top and bottom halves of the pillar, showcasing a planar configuration characteristic of a dotriacontapole.

We plot the additional mode profiles corresponding to the geometries shown in Fig. 2 of the manuscript, shown from Fig. S9 and on below.

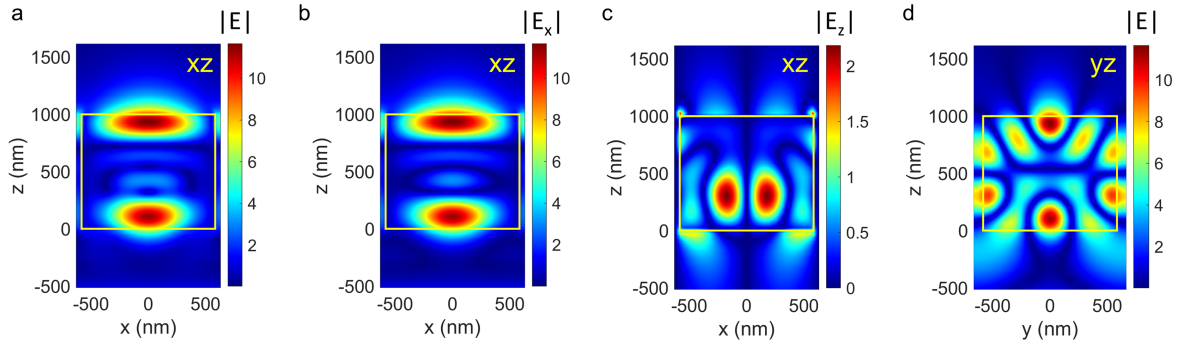


Figure S9: Field profiles for the x-period of $P_x = 1260$ nm. Panels a)–c) show the spatial distributions of a) the absolute electric field $|E|$, b) the absolute x-component $|E_x|$, and c) the absolute z-component $|E_z|$. These field profiles are plotted in the xz plane, which passes through the center of the Ge pillar and is parallel to the polarization of the incident light (x-polarization). Panel d shows the spatial distribution of $|E|$ in the yz plane, which also passes through the center of the Ge pillar but is perpendicular to the incident polarization. In this yz plane, only $|E_x|$ is nonzero ($E_y = E_z = 0$).

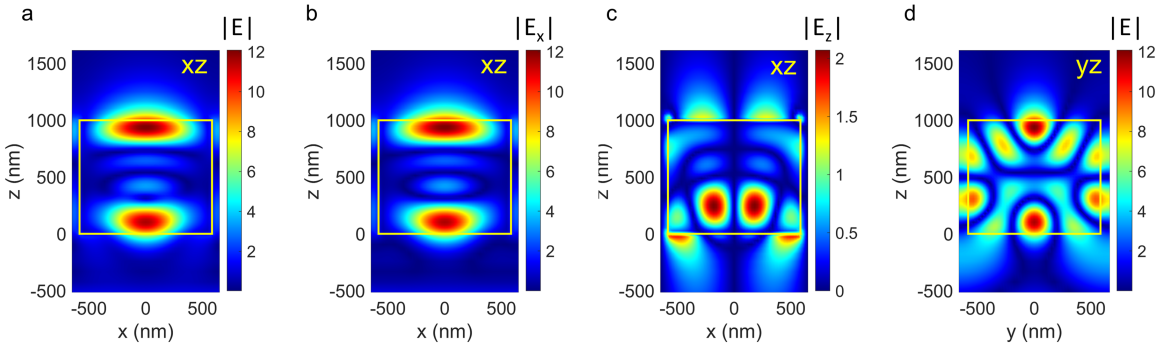


Figure S10: Field profiles for the x-period of $P_x = 1300$ nm. a), b), and c) display the spatial distribution of the absolute values of the electric field $|E|$, the absolute value of the x-component of the electric field $|E_x|$, and the absolute value of the z-component of the electric field $|E_z|$, respectively. a), b), and c) plot spatial field profiles in the xz plane, which passes through the center of the Ge pillar and is parallel to the polarization of the incoming light (x-polarization). In d), the spatial distribution of the absolute values of the electric field $|E|$ in the yz plane, which passes through the center of the Ge pillar and is perpendicular to the polarization of the incoming light (x-polarization). In the considered yz plane, $|E_x|$ is the only nonzero component ($E_y = E_z = 0$).

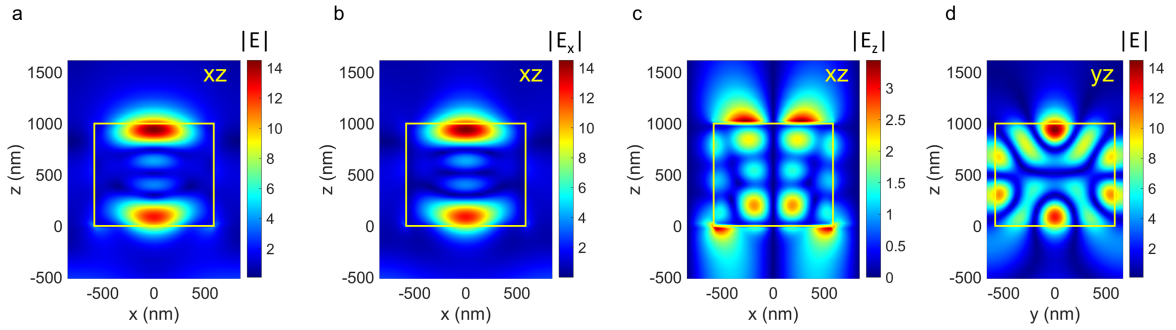


Figure S11: Field profiles for the x-period of $P_x = 1690$ nm. a), b), and c) display the spatial distribution of the absolute values of the electric field $|E|$, the absolute value of the x-component of the electric field $|E_x|$, and the absolute value of the z-component of the electric field $|E_z|$, respectively. a), b), and c) plot spatial field profiles in the xz plane, which passes through the center of the Ge pillar and is parallel to the polarization of the incoming light (x-polarization). In d), the spatial distribution of the absolute values of the electric field $|E|$ in the yz plane, which passes through the center of the Ge pillar and is perpendicular to the polarization of the incoming light (x-polarization). In the considered yz plane, $|E_x|$ is the only nonzero component ($E_y = E_z = 0$).

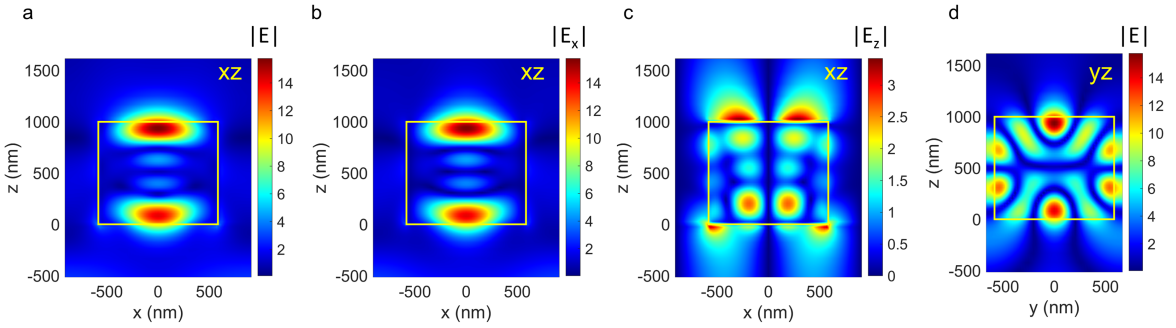


Figure S12: Field profiles for the x-period of $P_x = 1820$ nm. a), b), and c) display the spatial distribution of the absolute values of the electric field $|E|$, the absolute value of the x-component of the electric field $|E_x|$, and the absolute value of the z-component of the electric field $|E_z|$, respectively. a), b), and c) plot spatial field profiles in the xz plane, which passes through the center of the Ge pillar and is parallel to the polarization of the incoming light (x-polarization). In d), the spatial distribution of the absolute values of the electric field $|E|$ in the yz plane, which passes through the center of the Ge pillar and is perpendicular to the polarization of the incoming light (x-polarization). In the considered yz plane, $|E_x|$ is the only nonzero component ($E_y = E_z = 0$).

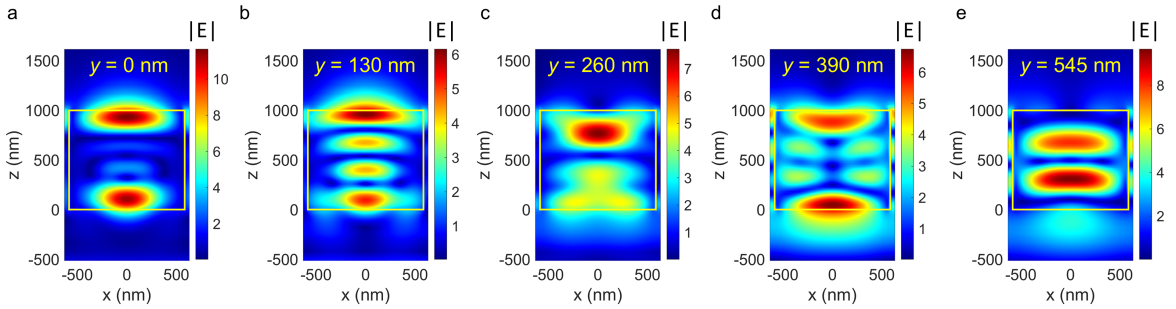


Figure S13: Field profiles for the x-period of $P_x = 1260$ nm. a), b), c) and d) display the spatial distribution of the absolute values of the electric field $|E|$ in xz planes, parallel to the incoming light polarization $|E_x|$, intersecting the y-axis at y = 0 nm, 130 nm, 260 nm, 390 nm, and 545 nm, respectively. Note that y = 0 nm marks the center of the pillar, while y = 583.5 nm marks the edge of the Ge pillar.

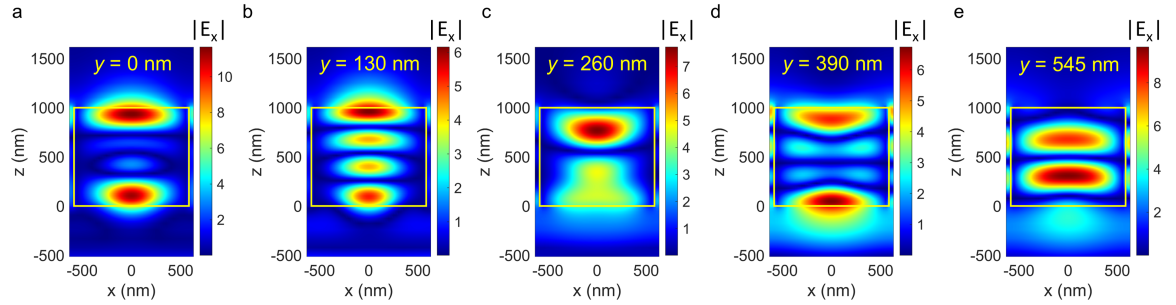


Figure S14: Field profiles for the x-period of $P_x = 1260$ nm. a), b), c) and d) display the spatial distribution of the absolute value of the x-component of the electric field $|E_x|$ in xz planes, parallel to the incoming light polarization $|E_x|$, intersecting the y-axis at y = 0 nm, 130 nm, 260 nm, 390 nm, and 545 nm, respectively. Note that y = 0 nm marks the center of the pillar, while y = 583.5 nm marks the edge of the Ge pillar.

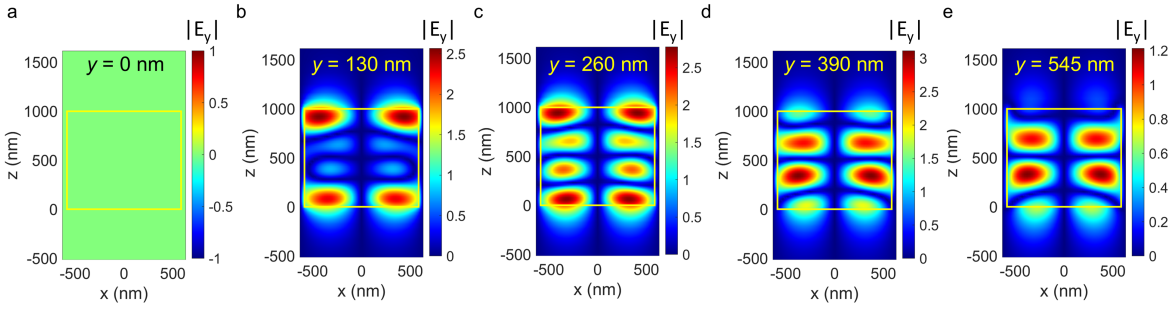


Figure S15: Field profiles for the x-period of $P_x = 1260$ nm. a), b), c) and d) display the spatial distribution of the absolute value of the y-component of the electric field $|E_y|$ in xz planes, parallel to the incoming light polarization $|E_x|$, intersecting the y-axis at y = 0 nm, 130 nm, 260 nm, 390 nm, and 545 nm, respectively. Note that y = 0 nm marks the center of the pillar, while y = 583.5 nm marks the edge of the Ge pillar.

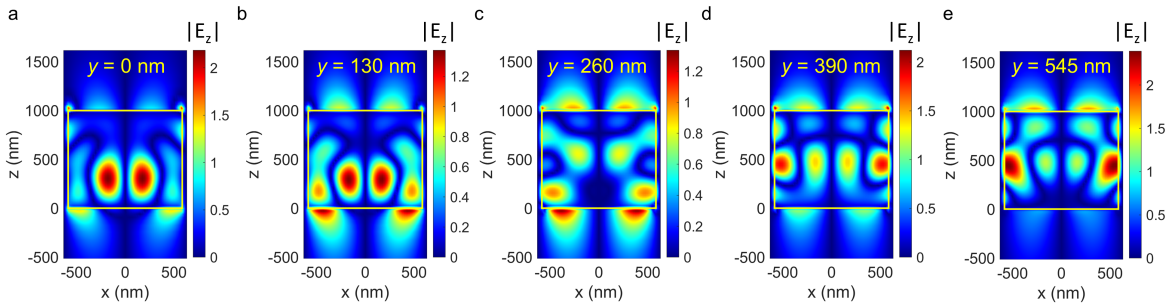


Figure S16: Field profiles for the x-period of $P_x = 1260$ nm. a), b), c) and d) display the spatial distribution of the absolute value of the y-component of the electric field $|E_z|$ in xz planes, parallel to the incoming light polarization $|E_x|$, intersecting the y-axis at y = 0 nm, 130 nm, 260 nm, 390 nm, and 545 nm, respectively. Note that y = 0 nm marks the center of the pillar, while y = 583.5 nm marks the edge of the Ge pillar.

3 Zeros and poles on the complex frequency plane

Recent work [4] highlights the role of zeros and poles of the transmission amplitude in phase modulation. It illustrates that in order for the resonance to span a full 2π phase range, the zero should be above the real frequency line such that the branch cut between the zero and the pole forms an intersection with the real frequency line. We will now show that achieving the condition of the complex transmission amplitude circle encircling the origin ($R^2 - |\mathbf{C}|^2 > 0$) is mathematically equivalent to having the transmission zero move upwards into the upper complex plane from the real frequency axis. Equation 1 in the main paper can be rearranged as follows:

$$\mathbf{t} = t + \frac{2i\sqrt{\gamma_1\gamma_2}}{(\omega-\omega_0)+i\gamma} = \frac{t(\omega-\omega_0)+it\gamma+2i\sqrt{\gamma_1\gamma_2}}{(\omega-\omega_0)+i\gamma} = t\frac{\omega-(\omega_0-i(\gamma+\frac{2\sqrt{\gamma_1\gamma_2}}{t}))}{\omega-(\omega_0-i\gamma)} \equiv A\exp(iB\omega)\frac{\omega-\omega_z}{\omega-\omega_p}$$

where the Weierstrass expansion form is shown on the utmost right. From the above we can see that the direct transmission scattering parameter t (complex-valued) corresponds to the term $A\exp(iB\omega)$, where the very slowly varying nature of t with respect to the frequency ω (compared to the resonance term) allows us to assume it is constant in the vicinity of the resonance ($B\omega \approx B_0, \rightarrow t \equiv A\exp(iB_0)$). The location of the complex zero is given by $\omega_z \equiv \omega_0 - i(\gamma + \frac{2\sqrt{\gamma_1\gamma_2}}{t})$, and the location of the complex pole, similarly, is given by $\omega_p \equiv \omega_0 - i\gamma$.

If the transmission zero moves up into the positive imaginary half-plane in the complex frequency space, it means that the imaginary component of the complex zero becomes positive: $\mathbf{Im}[\omega_z] = -\mathbf{Re}[\gamma + \frac{2\sqrt{\gamma_1\gamma_2}}{t}] > 0$ (Notice that the $\mathbf{Re}$ part is necessary because the term $\gamma + \frac{2\sqrt{\gamma_1\gamma_2}}{t}$ itself is complex-valued due to the complex t). Then rearranging $-\mathbf{Re}[\gamma + \frac{2\sqrt{\gamma_1\gamma_2}}{t}] > 0$ gives:

$$\mathbf{Re}[\gamma + \frac{2\sqrt{\gamma_1\gamma_2}}{t}] = \mathbf{Re}[\frac{2t^*\sqrt{\gamma_1\gamma_2}}{|t|^2} + \gamma] = \frac{2\sqrt{\gamma_2\gamma_2}}{|t|^2}\mathbf{Re}[t^*] + \gamma = \frac{2\sqrt{\gamma_1\gamma_2}}{|t|^2}\mathbf{Re}[t] + \gamma < 0 \tag{S29}$$

where the relation $\mathbf{Re}[t^*] = \mathbf{Re}[t]$ was used. Then dividing Eq. S29 by γ and multiplying by $-|t|^2$ gives us $-2\frac{\sqrt{\gamma_1\gamma_2}}{\gamma}\mathbf{Re}[t] - |t|^2 > 0$, which, from Eq. S21, is precisely the condition of $R^2 - |\mathbf{C}|^2 > 0$. Because the complex transmission pole is located below the real frequency axis due to $\mathbf{Im}[\omega_p] = -\gamma < 0$, the branch cut between the zero and the pole crosses the real frequency line, allowing for a full 2π phase change. It also naturally follows that having the condition of $R^2 - |\mathbf{C}|^2 = 0$ equates to having the transmission zero exactly on the real frequency axis, as in the case of two-port, single-resonance systems without loss or gain, and having the condition of $R^2 - |\mathbf{C}|^2 < 0$ indicates that the transmission zero is below the real frequency axis, failing to yield a full 2π phase change.

We will go further and qualitatively explain why the transmission zero cannot be on the real axis or exist as complex conjugate pairs, using the logical framework employed in the work [4].

The logic of the work was as follows. Suppose there is a transmissionless state for a two-port

system with its associated complex frequency, ω_{TZ}. If there's time-reversal symmetry, you could apply the time-reversal operation on to this state ω_{TZ} and get ω_{TZ}^*, which, in a two-port system, would also be a tranmissionless state. This means for a transmissionless state that either $\omega_{TZ} = \omega_{TZ}^*$ or $\omega_{TZ} \neq \omega_{TZ}^*$. Therefore, the transmissionless state complex frequencies ω_{TZ} exist either as real values or as complex conjugate pairs. If ω_{TZ} is a real value, there is zero transmission for that given real-frequency excitation, which prevents 2π phase range. If the transmissionless states exist as complex conjugate pairs, then one of the zero-pole pairs has its branch cut crossing the real frequency line, permitting 2π phase change. This spontaneous symmetry-broken state involves two resonances, the notable example being the Huygen metasurface involving multipoles of different symmetries satisfying the Kerker condition [5]. Additionally, there is the method of explicitly breaking the time-reversal symmetry to push the transmission zero away from the real axis. However, having intrinsic losses in the system pushes the zero downwards [6], which prevents the branch cut from crossing the real frequency line, so in the context of phase modulation, engineering the system to have a phase change of 2π is rather non-trivial unless sophisticated setups involving gain are employed.

Now let's apply the logical framework above to our system with additional diffraction ports. Suppose there is a transmissionless state ω_{TZ}. Due to the additional diffraction channels, this state entails having an incident beam coming through the incident port, having no light go through the transmission port, and also have light radiate out through the diffration ports as well. Because there's no intrinsic system loss, we can apply the time-reversal operation. After time-reversal, the system would now have the incident and the diffraction ports having light converging back into the system/resonator (all with intensities less than unity), and light being emitted out through the incident port with unity intensity. Although technically the transmission port does not carry any incoming or outgoing light, it is difficult to call this a 'transmissionless' state because the system requires destructive interference of the beams coming from both the incident AND the diffraction ports at the transmission port. If we were to only consider the incident and the transmission port through projection onto the incident/transmissive port subspace and disregard the diffraction ports, energy conservation would be violated, which would prevent the use of time-reversal symmetry. Therefore, in our system, the transmission zeros do NOT have to exist either on the real axis or as complex conjugate pairs.

We support our claim above with complex frequency plots showing the locations of the zeros and poles for our resonance in Fig. 2 of the main paper. The results are shown in Fig S8 below. The complex frequency sweep was done with the S4 RCWA software. Fig. S8a shows the complex frequency plot for the structure in Fig. 2 without diffraction (having P_x =1380 nm). As expected, the system is only a two-port system without diffraction ports, and therefore the transmission zero is indeed on the real frequency axis, with its exact location being $f_{\text{zero}} = 149.74 + 0i$ THz. This prevents the resonance from attaining a full 2π phase change. Fig. S8b shows the same system with a slightly larger period so that diffraction exists (P_x =1400 nm, the threshold period for diffraction is $P_{x,\text{threshold}} = 1388.9$ nm). The zero is now slightly displaced above the real axis, with its location being $f_{\text{zero}} = 149.75 + 0.01i$ THz. Fig. S8c shows the same structure with a much larger period $P_x = 1650$ nm, so that the zero

is displaced even higher, with its location being $f_{\text{zero}} = 149.75 + 0.06i$ THz. As all three complex frequency plots show, there is only a single zero-pole pair, signifying that only a single resonance is being utilized. For the diffraction cases, the $\arg t$ plots show the branch cut between the zero and the pole crossing the real frequency line, allowing for a full 2π phase change.

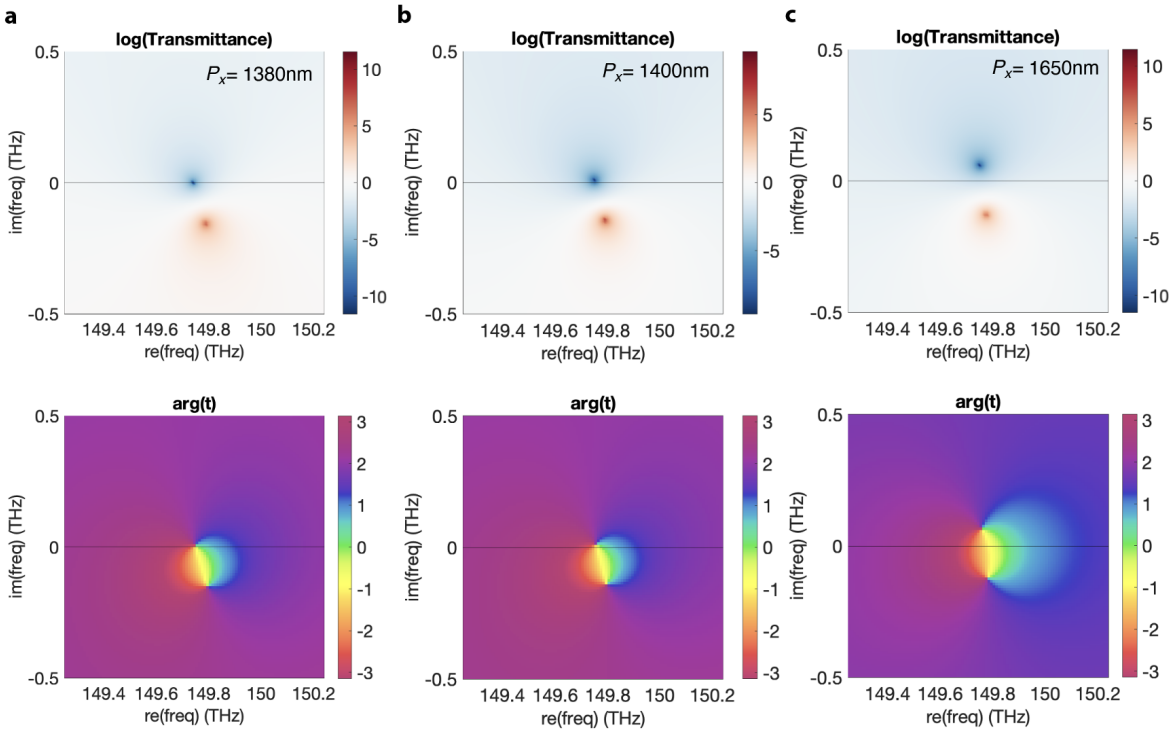


Figure S17: The complex frequency plot for $(\log |t|^2)$ and $\arg t$ for the structures (with differing P_x's) shown in Fig. 2 of the main paper. The common geometric parameters for all three cases **a**, **b**, **c** are: $P_y = 1328.6$ nm, Germanium ($n = 4$) pillar dimensions are 1167.7 nm (W) $\times$ 1167.7 nm (L) $\times$ 999 nm (H), and the substrate is silicon dioxide ($n = 1.44$). **a**. $P_x = 1380$ nm. **b**. $P_x = 1400$ nm **c**. $P_x = 1650$ nm.

4 Figure 3 Details

The resonance wavelengths λ_0 and the wavelength ranges used to plot Fig. 3 of the main manuscript were described in the caption of the figure. Here, we additionally the exact values for the complex direct transmission scattering parameters t_d, the radii R of the complex transmission amplitude circles, and the quality factors Q, for Fig. 3b-3f:

Figure	t_d	R	Q
3b.	$-0.6205 + 0.1513i$	0.329793	363.214
3c.	$-0.4561 + 0.1427i$	0.3352	375.949
3d.	$-0.5871 + 0.0608i$	0.370913	2943.99
3e.	$-0.4282 - 0.0154i$	0.448322	3254.32
3f.	$-0.4682 + 0.0205i$	0.455155	19864.6

Table S1: t_d, R, and Q values for the circles in Fig. 3

The coloring scheme of the circles in Fig. 3 is as follows. For the circles in Fig. 3b and 3c, the points on the circles were plotted with each point having an angular frequency difference of ($\Delta\omega = 3.64147 \times 10^9$ rad/s), and for the circles in Fig. 3d, 3e, and 3f, and angular frequency difference of ($\Delta\omega = 3.74177 \times 10^9$rad/s). The magnitude of the color change in terms of its RGB values from one point on the circle to its nearest neighboring point was the same for all the circles in Fig. 3b to 3f. This means that if a resonance has a higher quality factor, fewer points would be required to sweep around the circle (due to the narrow spectral linewidth), and therefore visually the circle would have a more spread-out rainbow coloring around the resonance point (the dark red point with a black outline). As can be confirmed in Table S1 above, the quality factor keeps increasing as the circles progress from Fig. 3b to 3f, with an order of magnitude difference between 3b, 3c and 3d, 3e (the spreading-out of rainbow coloring), and another big jump in the order of magnitude from 3d, 3e to 3f (indicated by the 3f circle becoming discretized, as the consecutive points become too far in distance from one another).

Figures S9 to S13 below show the spectral transmittance and phase line plots for the complex transmission amplitude curve/circles in Fig. 3a to 3f of the main manuscript, as well as the spectral reflection (R_{00}) and diffraction (R_{10} for $x-$directional first-order diffraction and R_{01} for $y-$directional first-order diffraction) line plots and the corresponding phase plots for the diffraction-enabled cases of Fig. 3c to 3f.

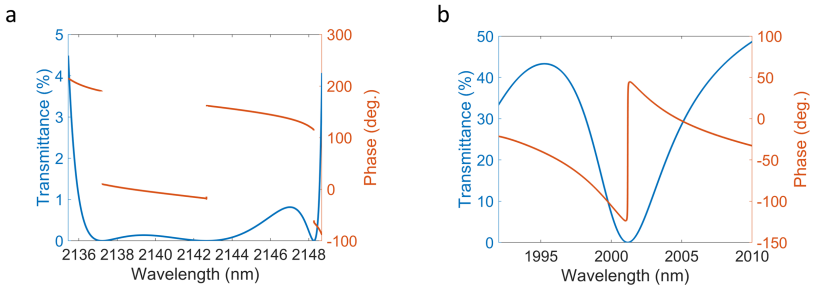


Figure S18: Phase and transmittance spectra corresponding to the complex amplitude plots shown in Fig. 3a and 3b of the manuscript. In (a), the transmission phase shows discontinuity. In (b), the phase extracted from full-wave simulations is continuous but spans from $-120°$ to $50°$, instead of the desired $0°$–$360°$.

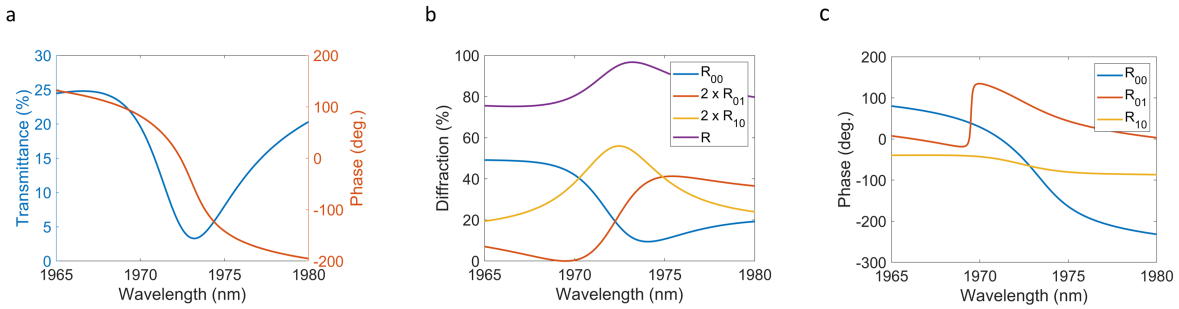


Figure S19: Phase and transmittance spectra corresponding to Fig. 3c.The effective wavelength within the substrate is now smaller than the metasurface period and the diffraction within the substrate is observed. (b) shows diffraction efficiencies in the normal direction R_{00}, y-direction R_{01}, and x-direction R_{10}. We plot $2 \times R_{01}$ and $2 \times R_{10}$ to account for $\pm 1^{\text{st}}$ diffraction orders. (c) plots the phases of the diffracted waves. R stands for the total Reflectance.

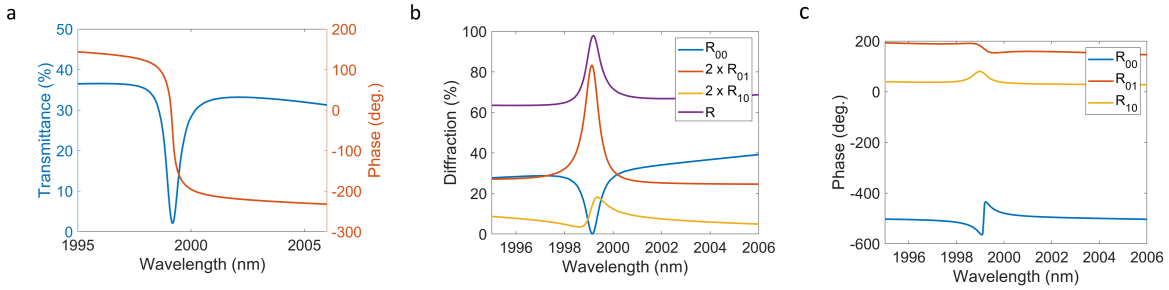


Figure S20: Same as above, corresponding to Fig. 3d.

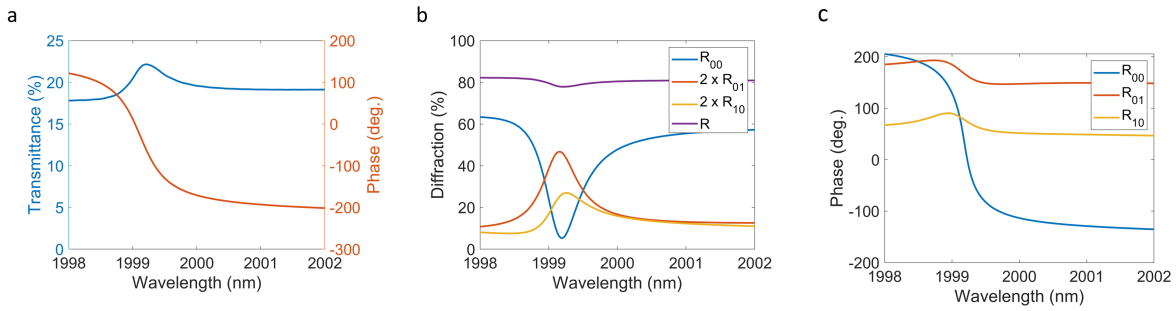


Figure S21: Same as above, corresponding to Fig. 3e.

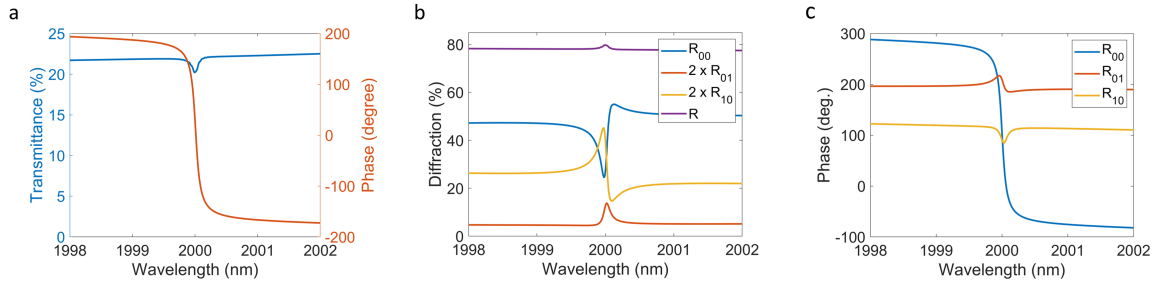


Figure S22: Same as above, corresponding to Fig. 3f.

5 Identifying Optimal Parameters

Here, we outline the process of identifying optimal parameters for centralized complex transmission amplitude circle with the largest radius. We consider our metasurface configuration excluding the ITO electrodes, not included in the simulation below. The assumed LN thickness is 339.6 nm, and the period in the x-direction is $P_x = 1959.2$ nm. The dimensions of the Ge pillar are $1175.5 \times 1175.5 \times 1005.7$ nm, where 1005.7 nm is the pillar height (along the z-direction). We simultaneously vary the width of the LN stripe and the period in the y-direction P_y. The wavelength range considered (1997–2001 nm) supports only one resonance. We plot the average transmittance ($(T_{\max} + T_{\min})/2$), transmittance variation ($T_{\max} - T_{\min}$), and a figure of merit (FOM):

$$\text{FOM} = \frac{T_{\max} - T_{\min}}{[(T_{\max} + T_{\min})/2]^{2.5}}$$

as a function of LN width and P_y below in Fig. S14. We choose geometric parameters that minimize the FOM. When minimized, the transmission spectra exhibit nearly constant transmission (phase-only control), while simultaneously optimizing for high transmittance (large circular radius for the complex transmission amplitude circle). As can be seen in Fig. S14c, there are multiple parameter sets that result in a high FOM, allowing us to select the one with the largest circular radius. Notice that the geometric parameters of the plot don't exactly match that of the parameters in Fig. 3 or Fig. 4 of the main manuscript. These plots are here to merely illustrate the process of optimal parameter selection.

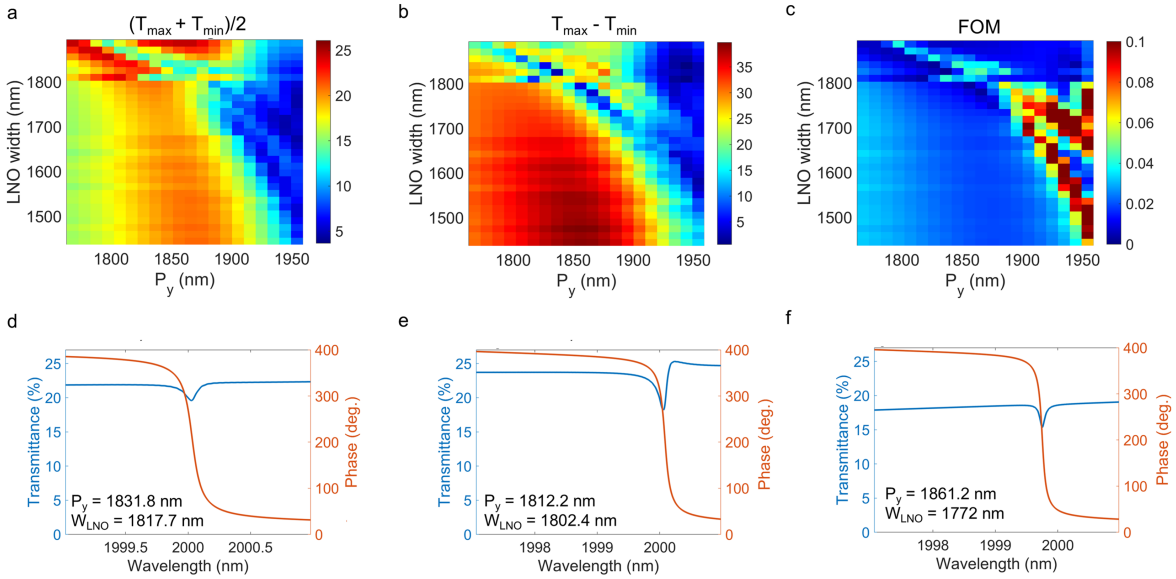


Figure S23: (a)–(c) plot average transmittance, transmittance variation, and the FOM as functions of LN width and P_y. In (a)–(c), the wavelength range is 1997–2001 nm. (d)–(f) show the transmission and phase spectra corresponding to the minimum FOM.

Let's now discuss the effects of the parameters w, P_y, and P_x. The width of the LN pedestal, w,

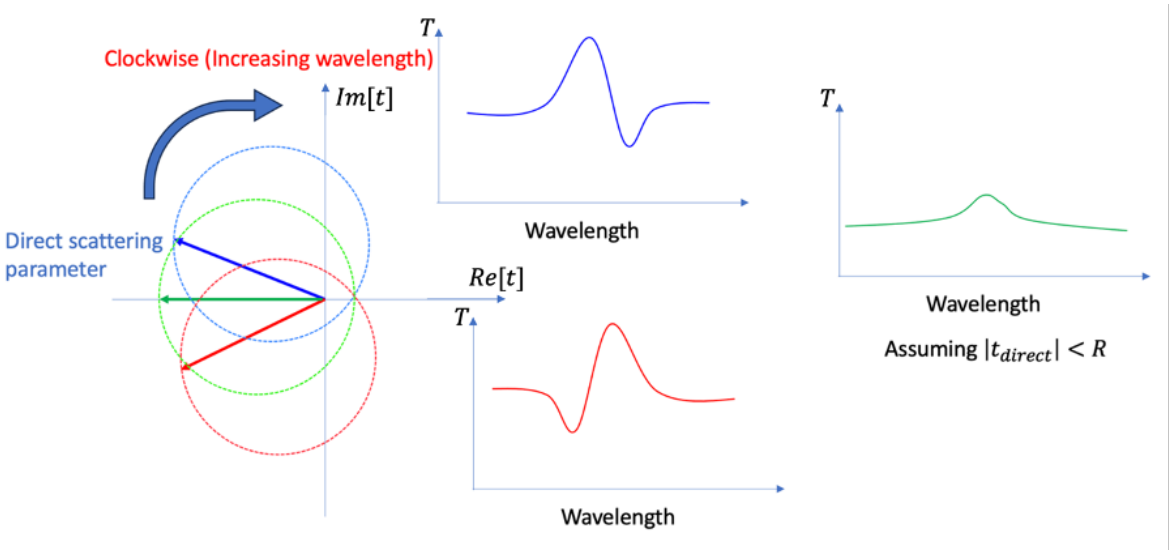


Figure S24: The effect of the relative phase of the direct transmittance scattering parameter on the Fano spectrum shape (each circle is traversed in the clockwise direction, according to the increasing wavelength). The complex transmission amplitude circles on the left correspond to the respective transmission intensity spectra on the right (mapping by $T = |t|^2$), which show transmittance as a function of wavelength. Three different colored cases correspond to three different $\theta_{\mathrm{td,rel}}$ values.

and the lattice period in the y-direction, P_y, both modify the optical confinement within each meta-atom by changing the size of the LN pedestal. Because the field is more weakly confined in the y–z plane than in the x–z plane, variations in P_y have a stronger influence on the modal effective index of the confined Mie resonance. This modal-index change shifts the resonance frequency and alters the relative phase between the direct transmission and the resonant scattering terms, producing the observed Fano-lineshape switching, shown in Fig. S24.

Indeed, based on the coupled-mode theory formalism, the relative phase of the direct transmission scattering parameter and the phase of the resonance term,

$$t = t_d + \frac{2i\sqrt{\gamma_1\gamma_2}}{(\omega-\omega_0)+i\gamma} = \left[|t_d|e^{i\theta_{\mathrm{td,rel}}} + \left|\frac{2i\sqrt{\gamma_1\gamma_2}}{(\omega-\omega_0)+i\gamma}\right|\right] e^{i\theta_{\mathrm{resonance}}},$$

define the shape of the Fano profile, where $\theta_{\mathrm{resonance}}$ is the phase of the resonance term (the value of which is not of importance for our objective), and $\theta_{\mathrm{td,rel}}$ is the relative phase difference of the t_d term from the resonance term. Changing the relative phase difference $\theta_{\mathrm{td,rel}}$ changes how much the circle is "offset" from the horizontal axis on the complex plane, which influences the Fano shape through the mapping

$$T = |t|^2.$$

Figure S24 above shows three different colored cases with different $\theta_{\mathrm{td,rel}}$ values.

In this sense, w and P_y act primarily as resonance-tuning parameters, controlling both the resonance frequency and $\theta_{\mathrm{td,rel}}$, the relative phase difference of the t_d term from the resonance term (Figs. S25

and S26). Changing P_x does not result in the Fano-shape switching (Fig. S27), but only changes the impedance and therefore $|t_d|$ (shown below).

At the same time, both P_x and P_y determine the lattice-diffraction behavior. When either period exceeds its respective diffraction threshold, additional diffraction ports open, modifying the overall impedance and coupling pathways. In Fig. 2 of the main manuscript, $P_y/n_{\text{substrate}}$ is subwavelength; hence, only P_x governs diffraction. In contrast, in Figs. 3 and 4, diffraction occurs in both x- and y-directions, so the metasurface behaves as a six-port system (one transmission, one reflection, and four diffraction ports).

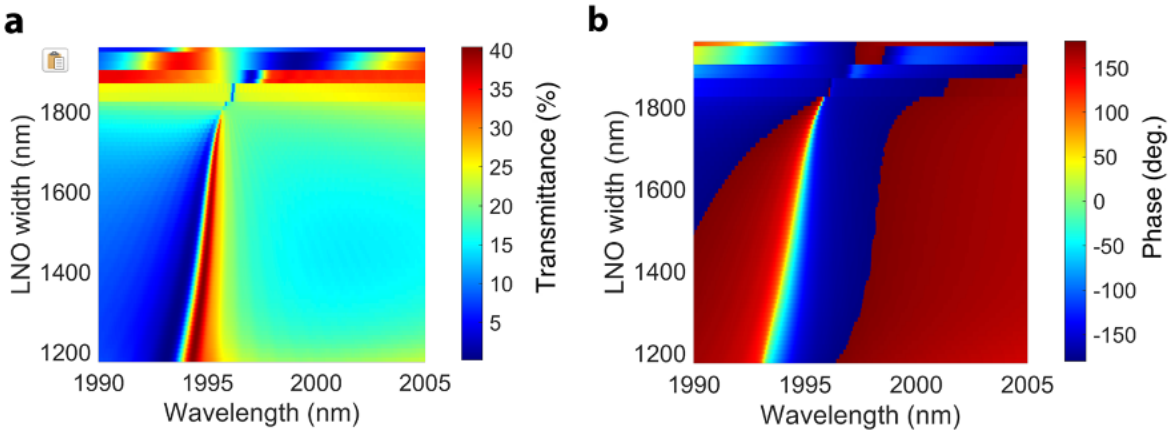


Figure S25: Transmittance **a** and phase of the transmitted light **b** as a function of the LN width w and wavelength. The geometrical parameters of the metasurface are the same as in Fig. 3f of the main manuscript. The geometrical parameters of the metasurface are chosen as follows: $P_x = 1959.2$ nm, $P_y = 1831.8$ nm, and the thickness of the LN layer is 339.6 nm. The dimensions of the pillars are 1175.5 nm $\times$ 1175.5 nm $\times$ 1502.0 nm (square base).

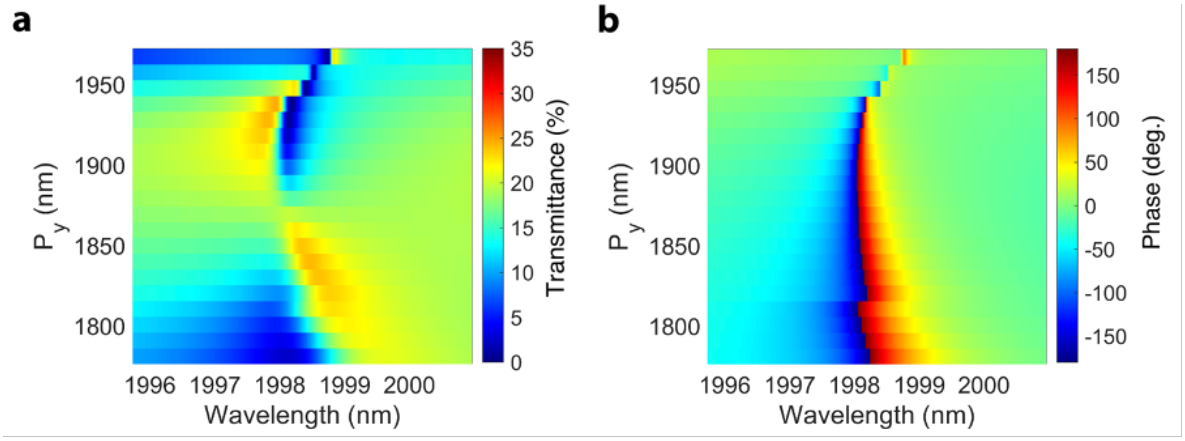


Figure S26: Transmittance **a** and phase of the transmitted light **b** as a function of the period in the y-direction P_y and wavelength. The geometrical parameters of the metasurface are chosen as follows: $P_x = 1959.2$ nm, the thickness of the LN layer is 263.8 nm, and the width of the LN layer is 1737.1 nm. The dimensions of the pillars are 1175.5 nm × 1175.5 nm × 1502.0 nm (square base).

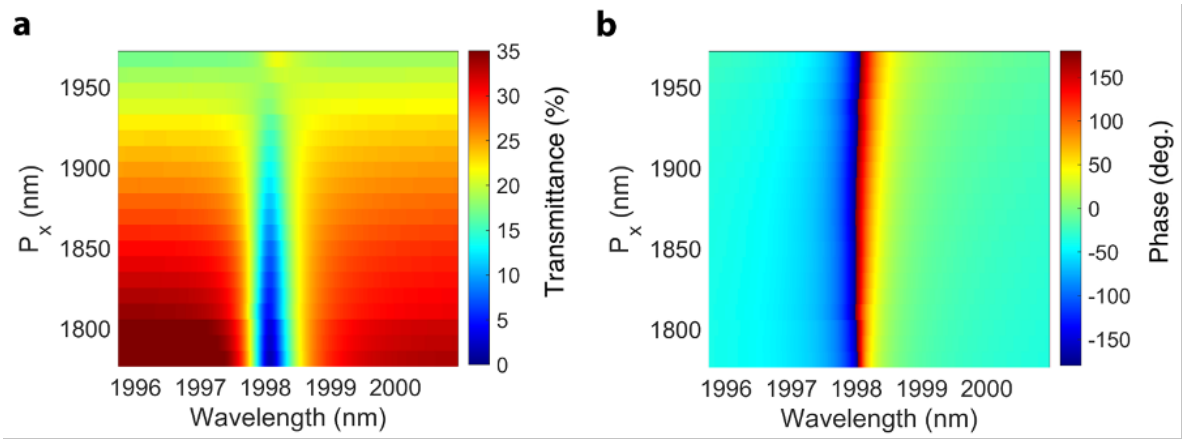


Figure S27: Transmittance **a** and phase of the transmitted light **b** as a function of the period in the x-direction P_x and wavelength. The geometrical parameters of the metasurface are chosen as follows: $P_y = 1831.8$ nm, the thickness of the LN layer is 263.8 nm, and the width of the LN layer is 1737.1 nm. The dimensions of the pillars are 1175.5 nm × 1175.5 nm × 1502.0 nm (square base).

6 Metasurfaces with continuous (unetched) LN films

Figure S15 below shows spectral transmittance and phase line plots for a metasurface configuration with a continuous LN film underneath the Ge pillars. These curves were among the best of the phase-only modulation results with such an unetched configuration. This is to illustrate that although the continuous LN film configuration below performs decently well in terms of transmissive phase-only modulation, etching of the LN to create the pedestal structure is necessary to achieve a near-optimal (close to the theoretical upper bound) results.

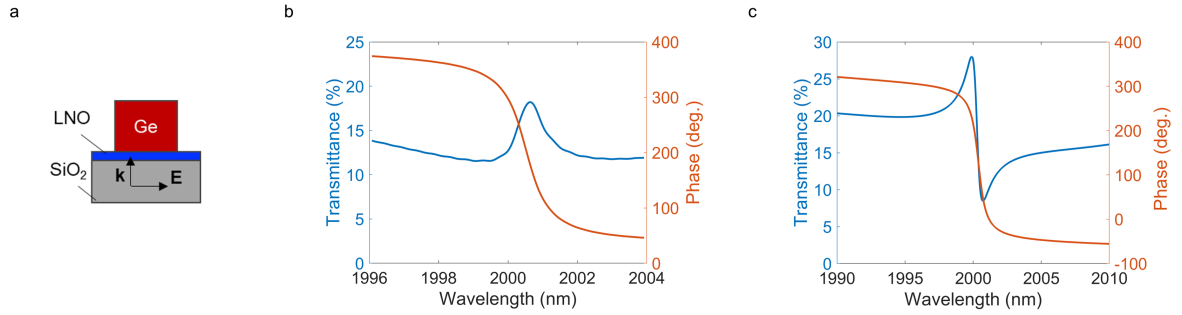


Figure S28: (a) Schematic of the metasurface unit cell with a continuous (unetched) LN film. (b) and (c) show transmittance and phase spectra for the following two geometries. For (b), the pillar height is 1005.9 nm, the pillar width and length are both 1175.8 nm, the LN thickness is 522.5 nm, P_x = 1806.7 nm, and P_y = 1858.8 nm. In c), the pillar height is 1009.2 nm, the pillar width and length are both 1179.5 nm, the LN thickness is 131 nm, P_x = 1793.4 nm, and P_y = 1914.2 nm. Simulations exclude electrodes, but we envision placing lateral transparent conducting electrodes on top of the LN films for practical realization.

7 Effects of finite ITO conductivity, and modulation speeds

When the ITO electrodes have finite conductivity, they behave as a series resistance that must charge the LN capacitor across the electrode gap. The electric field in the LN active region E_x is determined by the voltage dropped across the LN capacitor V_{LN}, i.e., $E_x = V_{\mathrm{LN}}/d$, where d is the electrode gap. Due to the finite conductivity of the ITO electrodes, part of the applied voltage V_s drops across the ITO electrodes. We can estimate the voltage dropped across the LN as [7]:

$$\left|\frac{V_{\mathrm{LN}}}{V_s}\right| = \frac{1}{\sqrt{1+(\omega R_s C)^2}}.$$

Here, ω denotes the angular modulation frequency, R_s is the total series resistance of the ITO electrodes, and C is the capacitance of the LN region between the electrodes. Importantly, the 3dB cutoff frequency is given by

$$f_{3\mathrm{dB}} = \frac{1}{2R_s C}.$$

Alternatively, one can write:

$$\left|\frac{E_{\mathrm{LN}}}{E_{\mathrm{ideal}}}\right| = \frac{1}{\sqrt{1+\left(\frac{f}{f_{3\mathrm{dB}}}\right)^2}}.$$

In our simulation, we describe the dielectric permittivity of ITO using the Drude model:

$$\varepsilon(\omega) = \varepsilon_\infty + \frac{\omega_p^2}{\omega^2 + i\omega\gamma}.$$

We take $\varepsilon_\infty = 3.9$, the plasma frequency $\omega_p = 5.224 \times 10^{14}$ rad/s, and the damping constant $\gamma = 1.256 \times 10^{14}$ rad/s. We compute the Drude conductivity of ITO as

$$\sigma = \frac{\varepsilon_0 \omega_p^2}{\gamma},$$

which yields a resistivity of

$$\rho = 5.2 \times 10^{-5}\ \Omega \cdot \mathrm{m}.$$

The resistance of a single ITO electrode is given by

$$R_0 = \frac{\rho L}{A},$$

where A is the cross-sectional area of the electrode, and $l = 40$ nm is the length of the electrode. The resistance of the two ITO electrodes in series is given as $R_s = 2R_0$.

In our estimate, we treat the LN layer, which is sandwiched between two ITO electrodes, as a parallel-plate capacitor. We calculate the capacitance according to

$$C_0 = \frac{\varepsilon_0 \varepsilon_r A}{d}.$$

Here, ε_r is the x-component of the LN DC permittivity, $\varepsilon_r = 27.9$, ε_0 is the dielectric permittivity of vacuum, A is the cross-sectional area of the LN, and $d = 1220$ nm is its width (the distance between the two ITO electrodes).

Given this information, we calculate the 3-dB modulation frequency from the RC constant:

$$R_s C_0 = \frac{2\rho\varepsilon_0\varepsilon_r l}{d}.$$

This yields a 3-dB frequency of approximately $f_{3\mathrm{dB}} \approx 190$ THz. Thus, these estimates show that up to modulation frequencies in the ∼THz regime, the ITO resistance imposes no limitation on the achievable index change of the LN.

In reality, parasitic resistance from the interconnects will significantly degrade the true 3-dB modulation frequency, and based on recent reports on LN-based electro-optic metasurfaces, speeds in the MHz range are realistically attainable [8].

We now address the problem of scalability in terms of the electrical control architecture. The current design implements a one-dimensional addressing scheme that enables dynamic wavefront shaping and beam steering along a single spatial direction. The lateral ITO electrodes on opposite sides of each LN block are biased in a manner similar to that demonstrated in our previous work [9], where we experimentally realized 96 individually addressable elements using edge-fed lateral biasing. This approach provides a straightforward and low-parasitic configuration that is well suited for compact device layouts.

In the present platform, the same concept can be extended to a much larger number of controllable elements by incorporating via-connected buried interconnects or row–column multiplexed addressing. In this architecture, one lateral ITO electrode can remain continuous and serve as a shared reference, while the opposite electrode is segmented and connected vertically through vias to buried routing layers. The buried interconnects would conventionally be metallic (e.g., Ti/Au or W) to ensure low resistance and high-speed operation. However, heavily doped semiconductors or transparent conductive oxides could alternatively be used when optical transparency or full monolithic integration is desired. These buried layers are positioned well below the optical near-field region and therefore, in principle, their effect on the metasurface transmission or phase response can be minimal. Overall, this architecture provides a clear and practical path toward scalable electrical control without introducing additional optical loss or fabrication complexity.

8 Electrostatic Analysis

To further clarify the underlying physics, we performed additional electrostatic simulations using the Lumerical Device software package. As a representative case, we modeled the Si resonators presented in Figs. 4d–4e. For computational efficiency and without loss of generality, the Si structure was approximated as an infinitely long bar, and the ITO electrodes were replaced by Au (Fig. S25a). This simplified geometry accurately preserves the key electrostatic characteristics relevant to our device operation. In our electrostatic simulations, we simulate three metasurface elements (Fig. S25a), and the assumed geometrical dimensions are the same as in Fig. 4d–e of the main manuscript. Our device operates capacitively, and there is no direct current under applied bias.

In schematic S25a, "G" marks the ground electrodes while "V" marks the signal electrodes to which we apply 30 V. The spatial distribution of the absolute value of the DC electric field is shown in Fig. S25b. We observe a large electric field enhancement in the air gaps between the electrodes. At an applied voltage of 30 V, the peak absolute value of the electric field reaches 1.6 x 10^8 V/m. These electric field values exceed the commonly cited value of electrostatic breakdown in air, 3 MV/m. However, at nanometer-to-submicrometer separations, the breakdown field in air dramatically exceeds the familiar macroscopic limit of 3 MV/m because classical Paschen scaling fails and field-emission–assisted breakdown becomes dominant [10]. Wang et al. measured breakdown in 200–300 nm atmospheric nanogaps at 2–3 x 10^8 V/m, demonstrating the transition to field-emission-dominated behavior [11]. Similarly, Matthews (2023) reported atmospheric breakdown in 150–250 nm MEMS gaps at 2.3–3.3 x 10^8 V/m in experimental devices, corroborating that nanoscale breakdown fields can reach one to two orders of magnitude higher than the classical air value [12]. These findings establish that electrostatic breakdown in nanogaps cannot be predicted using traditional macroscopic rules and must account for nanoscale electron-emission physics. In summary, at an applied voltage of 30 V, we do not expect to observe electrostatic breakdown since the field is applied across a 200 nm-wide air gap. In general, when electrically creating smooth optical phase profiles, we expect a much weaker DC electric field in the air gap than the one depicted in Fig. S25b.

As seen in Fig. S25b, there is a significant penetration of the DC electric field into LN with the main electrostatic component being E_x. Using the spatial distribution of the x-component of the electric field we can calculate the change in the refractive index of the LN crystal, which we assume to be x-cut (Fig. S25c). In our calculation, we use the following expression for change in the x-component of the refractive index $\Delta n_x = n_x - 0.5 n_x^3 r_{33} E_x$ [13]. To observe the refractive index change more clearly, we fix the z-coordinate at $z = 0.112$ μm and plot Δn_x as a function of x (Fig. S25d). As seen in Fig. S25d, the observed maximal refractive index change ranges between 2.8×10^{-3} and 5×10^{-3}. The sign of Δn_x is reversed upon switching the polarity of E_x. Comparing Fig. 4e of the main manuscript and Fig. S25d, we observe that at an applied bias of 30 V, we expect a dynamically tunable phase shift of 240°, which is large enough for performing beam steering or complex wavefront shaping. Increasing

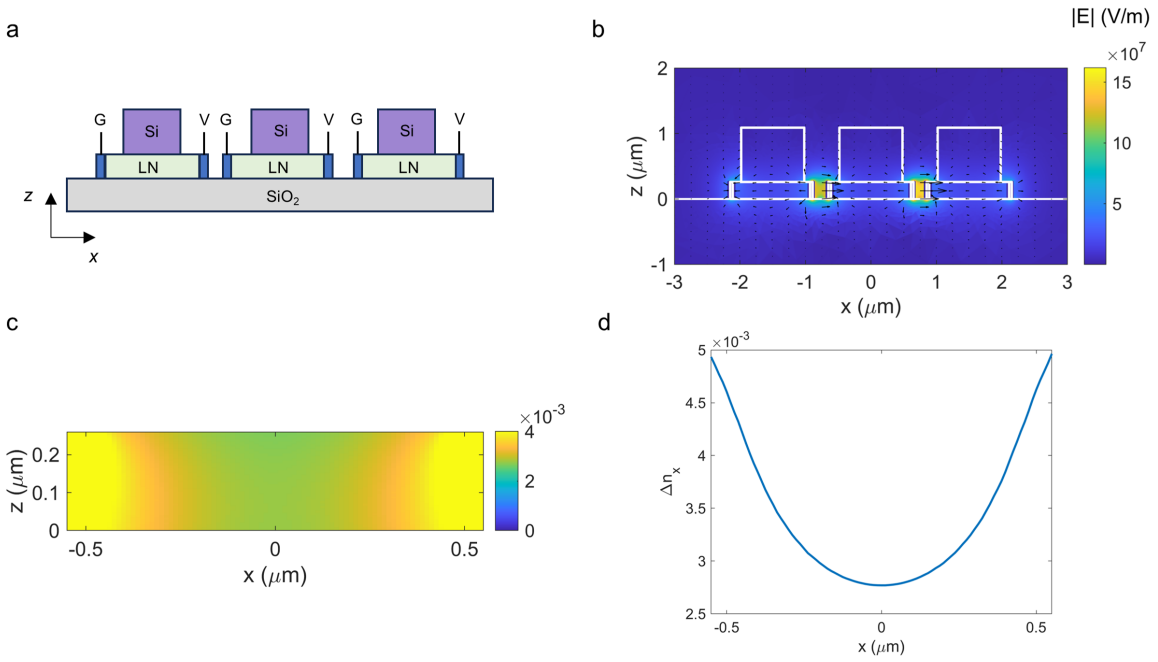


Figure S29: (a) Schematic of the structure modeled in electrostatic simulations. "G" shows ground electrodes while the voltage applied to signal electrodes is V = 30 V. The geometrical parameters of the structure are described in the caption of Figure 4 of the manuscript. (b) Spatial distribution of the absolute value of the DC electric field $|E|$. (c) Spatial distribution of the change of the x-component of the LN refractive index Δn_x, plotted within the bounds of the central LN layer. (d) The LN refractive index change Δn_x as a function of the x-coordinate at z = 112 nm.

the applied bias to 50 V would increase the dynamically tunable phase shift range to 300° while the electric field in the air gap will approach the electrostatic breakdown limit, adopting values on the order of 2.5×10^8 V/m.

It is also worth noting that in many wavefront shaping applications, the potential difference between neighboring ITO electrodes can be quite small. In general, when electrically creating smoother phase profiles, we expect a much weaker DC electric field in the air gap than the one depicted in Fig. S25b.

As an example, we employ the voltage application configuration shown in Fig. S26a, where there is no potential difference between adjacent electrodes. In Fig. S26a, we assume the applied bias voltage equals V = 50 V. In this case, we observe no significant electric field in the air gaps between neighboring electrodes (Fig. S26b). Notably, for neighboring metasurface elements, the x-component of the electric field has opposite polarity. This indicates that the LN refractive index change under neighboring metasurface elements shifts in opposite directions.

The voltage application configuration shown in Fig. S26a yields a two-level phase grating. To achieve full suppression of the zeroth diffraction order, the relative phase of light transmitted by neighboring metasurface elements should be equal to 180°. A relative phase difference of 180° is achieved at an applied bias of 20 V (Fig. S27). In general, when creating smoother phase profiles, we

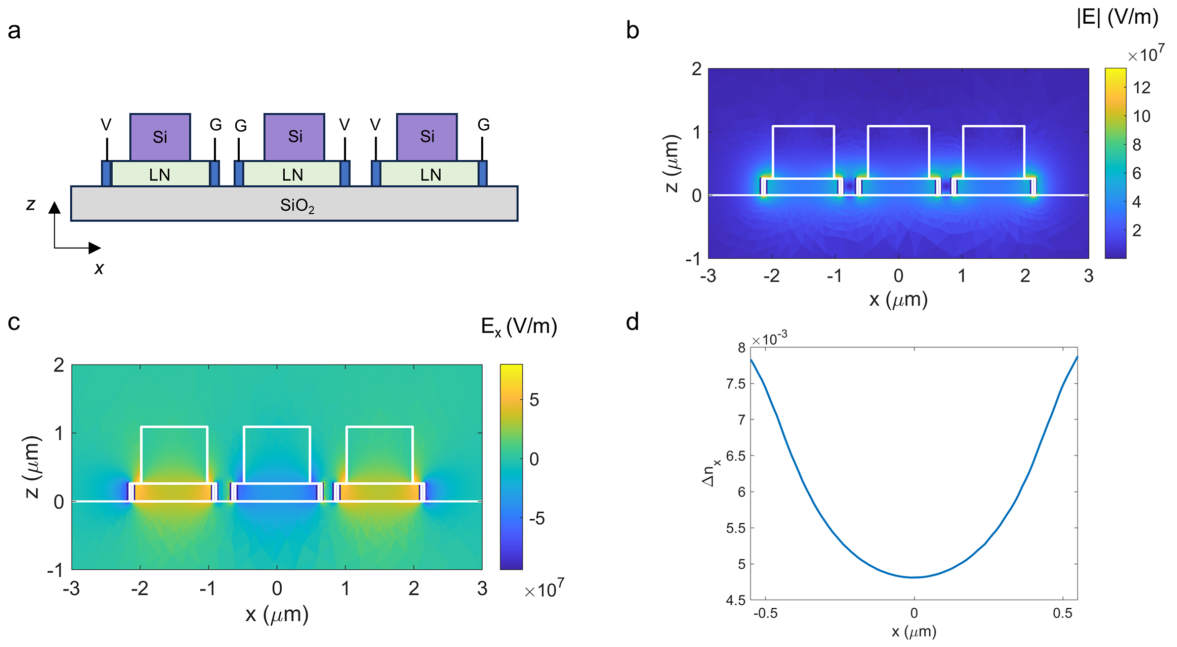


Figure S30: (a) Schematic of the structure modeled in electrostatic simulations. "G" shows ground electrodes while the voltage applied to signal electrodes is V = 50 V. The geometrical parameters of the structure are described in the caption of Figure 4 of the manuscript. (b) Spatial distribution of the absolute value of the DC electric field $|E|$. (c) Spatial distribution of the change of the x-component of the DC electric field E_x. (d) The LN refractive index change Δn_x as a function of the x-coordinate at z = 112 nm.

expect a much weaker DC electric field in the air gap than the one depicted in Fig. S25b.

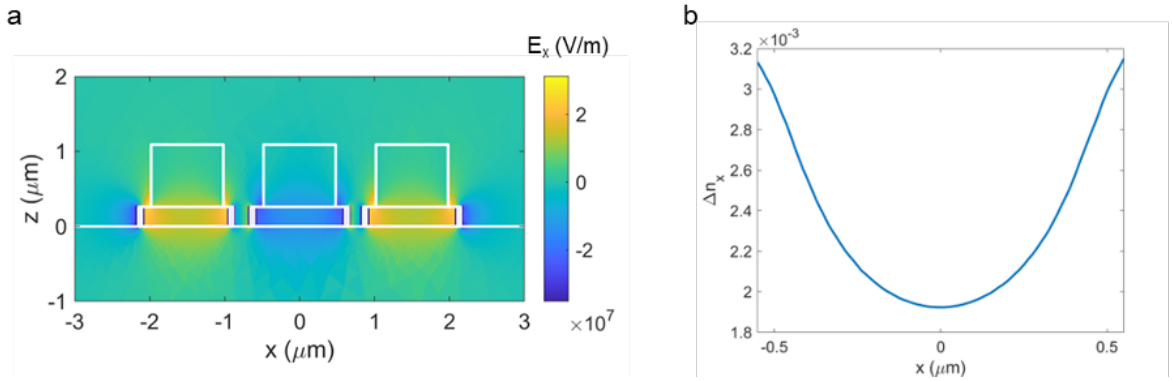


Figure S31: (a) Spatial distribution of the change of the x-component of the DC electric field E_x. (b) The LN refractive index change Δn_x in the central LN layer as a function of the x-coordinate at z = 112 nm. The geometrical structure and voltage application configuration are the same as in Fig. S26a.

9 Illumination from the air side

We would like to now address the problem of what would happen if the incident light was coming from the air side instead of the substrate side. To state the results first, both illumination conditions are possible: the case of incidence from air and the case of incidence from the substrate. The case of light incidence from the substrate side, in our view, is more interesting for future applications since it mimics the scenario when the metasurface is integrated with a chip-scale light source such as vertical-cavity surface-emitting lasers (VCSELs) or photonic-crystal surface-emitting lasers (PCSELs).

To address this question, we simulated the scenario in which the light source is located above the metasurface, i.e., illumination from the air side. The considered metasurface consists of an array of Ge pillars on a silica substrate with geometrical parameters identical to those assumed in Fig. 2. It is worth noting that, in this case, the transmitted light will be diffracted for periods exceeding $P_x > (\lambda_0/n_s)$, where λ_0 is the wavelength of the incident light and n_s is the refractive index of the substrate. On the other hand, when the illumination comes from within the substrate, the transmitted light will be diffracted only for periods $P_x > \lambda_0$, offering greater flexibility with the choice of the metasurface period. In the considered scenario, the diffraction occurs for periods $P_x > 1389$ nm.

Our results for air-side illumination are summarized below. As seen in Fig. S32, in reflection we observe continuous phase variation covering the range approximately from 0 to 360°, both in the cases of the presence and absence of diffraction channels. On the other hand, as confirmed by our analytical theory, we observe a limited phase variation in transmission when no diffraction is present (Fig. S32b). As seen in Fig. S32b, the complex transmission circle does not encircle the origin, indicating a limited phase variation in transmission. However, this situation changes when we increase the period of the metasurface and introduce diffraction within the substrate. In that case, we observe that the light in the zeroth diffraction order, $\arg(T_{00})$, exhibits a phase variation from 0 to 360° in transmission (Fig. S32c). Interestingly, the phase variation of the first diffraction order, $\arg(T_{10})$, remains limited (Fig. S32d). As seen in Fig. S32d, the complex diffraction coefficient of the first diffraction order does not encircle the origin, indicating a limited accessible phase range.

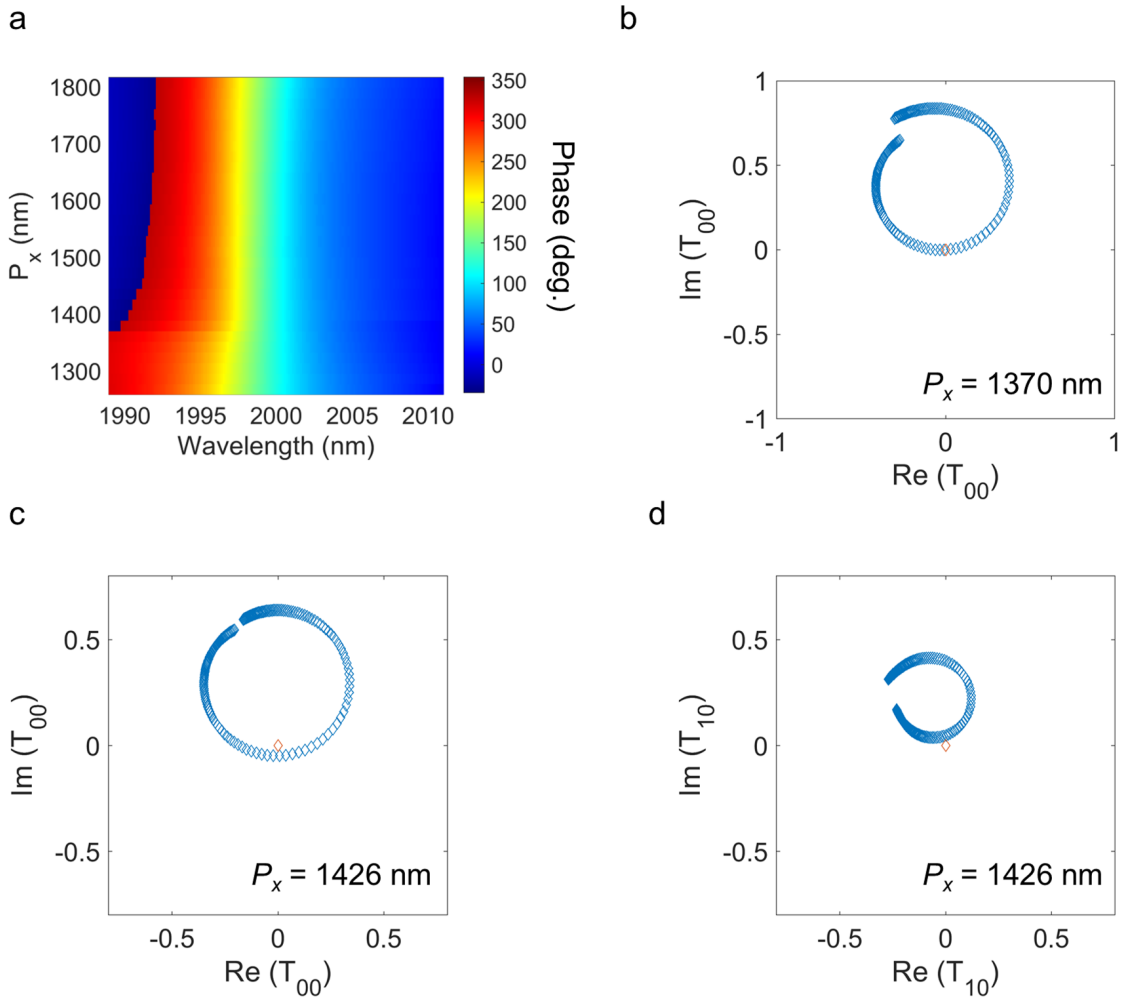


Figure S32: Behavior of the metasurface under illumination from the air. **a** Phase of the reflected light as a function of wavelength and the period in the x-direction, P_x. **b** Complex transmission coefficient for $P_x = 1370$ nm when no diffraction in transmission is observed (the case of a two-port system). **c**, **d** Complex transmission coefficients T_{00} and T_{10} corresponding respectively to the zeroth-order (direct transmission) and first-order diffracted channels, for $P_x = 1426$ nm where diffraction appears in transmission (four-port system). In **b** and **c**, the wavelength varies between 1989 nm and 2011 nm. The y-period P_y is taken as $P_y = 1328.6$ nm.

10 Results with varying material losses

In our metasurface design, we employ the following materials: SiO_2, Ge, Si, lithium niobate (LN), and indium tin oxide (ITO). In our simulations, SiO_2, Ge, Si, and LN are assumed to be lossless, which is a reasonable assumption in the considered mid-infrared wavelength range. The losses of ITO are accounted for in the simulation summarized in Fig. 4 of the main manuscript.

Based on highly sensitive measurements reported in the literature [14], in the wavelength range of interest, the extinction coefficient of LN ranges between $k = 1.6 \times 10^{-9}$ and $k = 2.4 \times 10^{-7}$. These extinction coefficients are sufficiently low and can be neglected in our simulations. SiO_2 is typically considered highly transparent; however, it may potentially exhibit absorption because impurities may be introduced during fabrication [15]. In the wavelength range of interest, the extinction coefficient can adopt values between $k = 10^{-7}$ and $k = 2 \times 10^{-5}$ [15]. However, since the electric field is mainly concentrated in the high-Q resonator with some amount leaking into the LN layer, we do not expect that these modest losses in SiO_2 would affect the optical performance of the metasurface.

On the other hand, the optical response of the metasurface would be most sensitive to potential losses in the high-index pillar. Notably, the extent of the effect of losses on the optical response depends on the quality factor of the resonance, with lower-Q structures exhibiting higher tolerance toward losses. Experimentally measured optical constants of Ge have been reported in the literature [16, 17]. In the wavelength range of interest, the reported extinction coefficient values are either zero or negligibly small. It is worth mentioning, however, that the reported refractive index values were measured via spectroscopic ellipsometry, which is not able to resolve accurately such small extinction coefficients. Thus, high-accuracy measurements for the optical constants of Ge in the mid-IR wavelength range are needed. Based on the literature reports, the extinction coefficient of Si in the wavelength range of interest can be negligibly small, with $k = 10^{-11}$ [18]. Nevertheless, it is interesting to understand how potential optical losses would affect the optical response of the metasurface.

To investigate the effect of losses on optical performance, we re-simulated the metasurface reported in Fig. 3 for different assumed extinction coefficients of Ge. The results are summarized in Figs. S33–S35, which show the transmittance and phase of the transmitted light for each geometry. In Fig. S33 (same geometry as Fig. 3d), the transmittance decreases steadily with increasing extinction coefficient. When k reaches $k = 2\times10^{-4}$, the accessible phase range is dramatically reduced. In Fig. S34 (geometry of Fig. 3e), the transmittance remains reasonably high even for k up to $k = 1 \times 10^{-4}$. A noticeable shift in the spectral phase response occurs only when k reaches $k = 8 \times 10^{-4}$. In Fig. S35 (geometry of Fig. 3f), the optical response is much more sensitive to loss. This higher susceptibility is consistent with the larger quality factor of the resonance compared to that in Fig. 3e. For example, the minimum transmittance drops to 10% for $k = 2 \times 10^{-5}$, and the phase variation becomes severely limited when k reaches $k = 2 \times 10^{-4}$.

Finally, we clarify the assumptions regarding the optical constants of ITO assumed in our work.

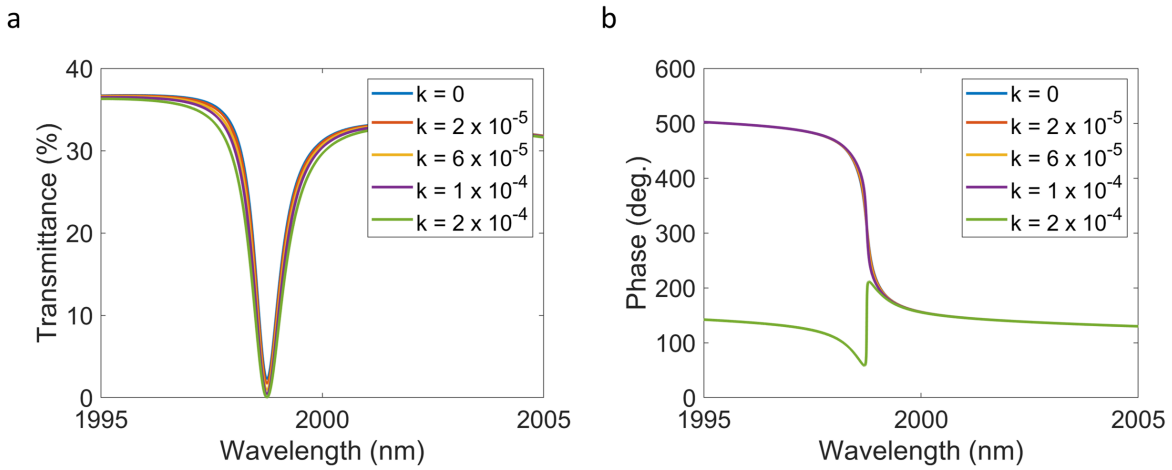


Figure S33: Influence of Ge resonator loss on metasurface performance. The geometrical parameters are the same as in Fig. 3d. **a** Transmittance and **b** phase of the transmitted light are shown for different assumed values of the Ge extinction coefficient, $k = \mathrm{Im}(n_{\mathrm{Ge}})$.

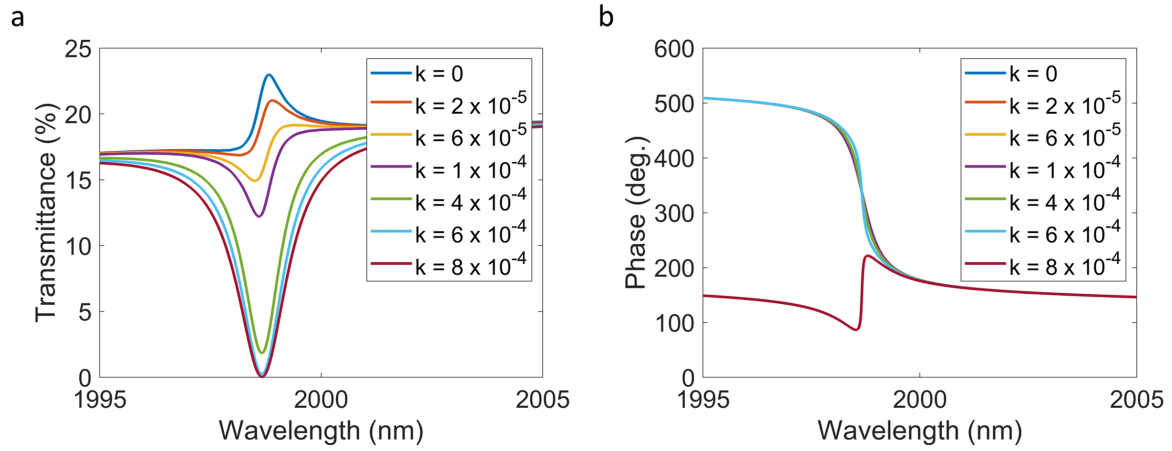


Figure S34: Influence of Ge resonator loss on metasurface performance. The geometrical parameters are the same as in Fig. 3e. **a** Transmittance and **b** phase of the transmitted light are shown for different assumed values of the Ge extinction coefficient, $k = \mathrm{Im}(n_{\mathrm{Ge}})$.

In our simulations, the dielectric permittivity of ITO has been described using the Drude model [19]:

$$\varepsilon(\omega) = \varepsilon_\infty - \frac{\omega_p^2}{\omega^2 + i\omega\gamma}. \tag{1}$$

In our simulations, the constant ε_∞ is taken as $\varepsilon_\infty = 3.9$, the plasma frequency as $\omega_p = 5.224 \times 10^{14}$ rad/s, which corresponds to an ITO carrier density of 3×10^{19} cm^{-3}. The damping constant is taken as $\gamma = 1.256 \times 10^{14}$ rad/s.

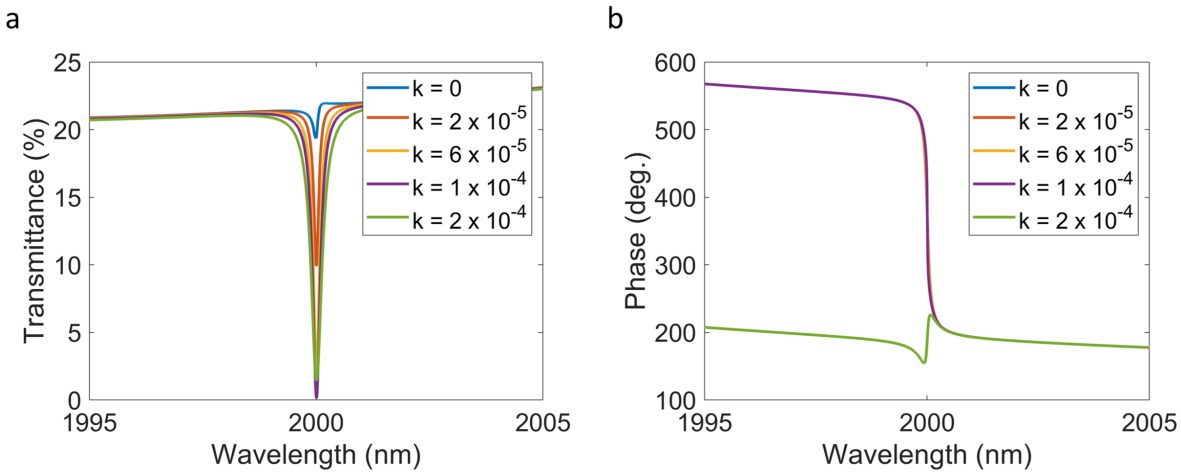


Figure S35: Influence of Ge resonator loss on metasurface performance. The geometrological parameters are the same as in Fig. 3f. **a** Transmittance and **b** phase of the transmitted light are shown for different assumed values of the Ge extinction coefficient, $k = \mathrm{Im}(n_{\mathrm{Ge}})$.

11 Dispersion in dielectrics

In our simulations, we assumed constant refractive index values for all materials except for ITO, whose dispersion has been properly accounted for (see the response to the previous question). Indeed, in the considered mid-IR wavelength range, Si, Ge, LN, and SiO_2 exhibit extremely low losses and are practically nondispersive. Moreover, since the reported simulations are performed over a narrow wavelength range, typically around 10 nm, the refractive index variation of the constituent materials is rather modest.

For example, based on the literature report [17], the real part of the Ge refractive index varies between 4.00062 and 3.99946 as the wavelength ranges between 3050 nm and 3090 nm. The reported imaginary part of the refractive index (extinction coefficient) is zero [17].

Using the reported modest refractive index variation of Ge, we re-simulated Fig. 4b of the manuscript. However, since the dispersion has been introduced into the simulation, the software package assigns nonzero values of around 8.9×10^{-10} to the extinction coefficient of Ge. As seen in Fig. S36, accounting for the dispersion of Ge in our simulation does not affect the simulation result. Indeed, Figs. 4b and S36 are indistinguishable.

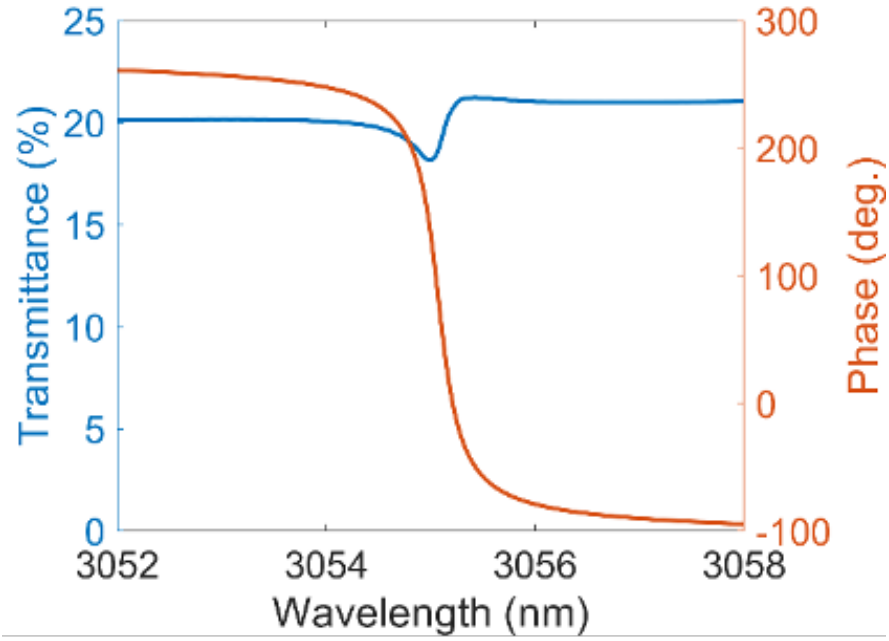


Figure S36: Transmittance and phase spectra of the metasurface shown in Fig. 4. We assume that the high-index pillar is comprised of Ge. The dispersion of the Ge refractive index has been accounted for in the simulation.

12 Sensitivity Analysis

In our manuscript, the geometrical parameters of the metasurface are reported with sub-nanometer precision to represent our simulation setup accurately. However, for achieving the target optical behavior, such precision is not needed. To verify this, we carried out a sensitivity analysis of the geometric parameters below.

Starting from the optimized metasurface design shown in Fig. 3f and Fig. 4b, we systematically varied the geometrical parameters to determine the range over which the flat-transmittance feature, together with the associated phase variation, is preserved. We varied the following geometrical parameters: period in the y-direction P_y, period in the x-direction P_x, the pillar height h, the LN thickness t, and the LN width w. Additionally, we assessed how changing the width of the ITO electrodes affects the performance of the metasurface.

We identified that the spectrally flat nature of the resonance is preserved for the following parameter ranges:

$$P_y \in [1826 \text{ nm}, 1834 \text{ nm}],$$
$$P_x \in [1960 \text{ nm}, 1980 \text{ nm}],$$
$$h \in [1004 \text{ nm}, 1006 \text{ nm}],$$
$$w \in [1790 \text{ nm}, 1805 \text{ nm}],$$
$$t \in [280 \text{ nm}, 340 \text{ nm}],$$
$$\text{ITO width} \in [30 \text{ nm}, 50 \text{ nm}].$$

The optical response of the metasurface is most sensitive to variations in the high-index pillar height h. Nevertheless, the pillar height does not need to be specified with sub-nanometer precision.

Below, we present the simulation results of our sensitivity analysis.

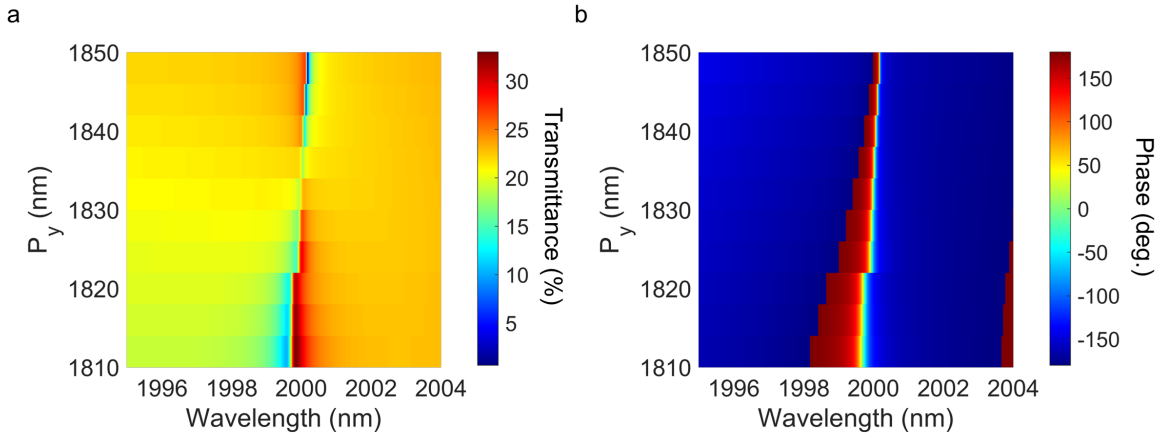


Figure S37: Transmittance **a** and phase of the transmitted light **b** as a function of the period in the y-direction P_y and wavelength. The geometrical parameters of the metasurface are the same as in Fig. 3f of the manuscript.

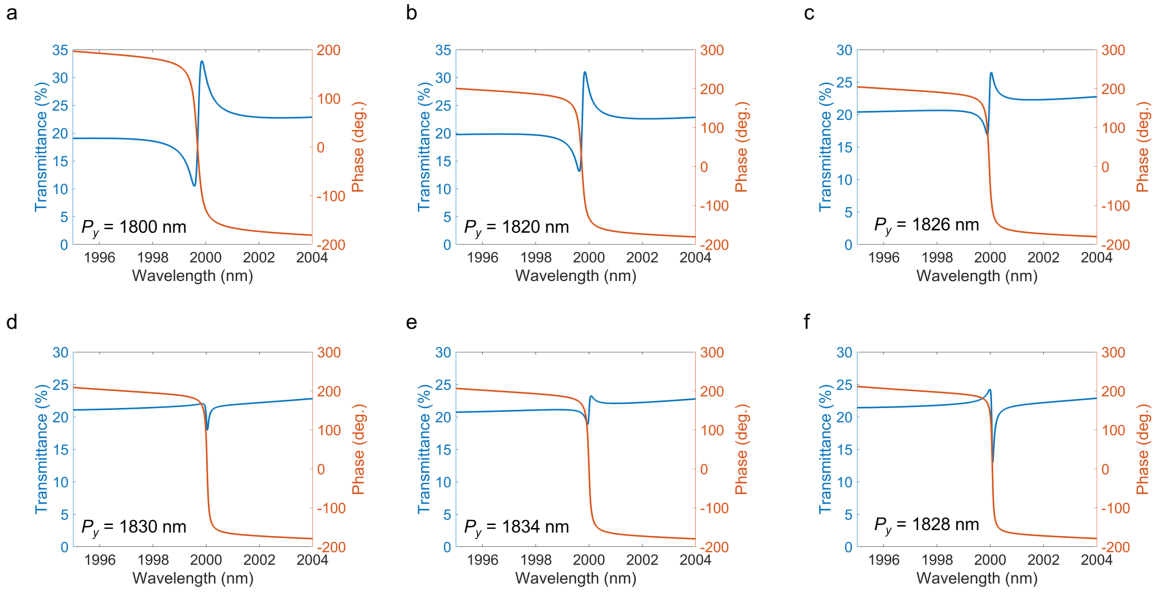


Figure S38: Transmittance and phase of the transmitted light as a function of wavelength for different values of the period in the y-direction P_y. The geometrical parameters of the metasurface are the same as in Fig. 3f. An almost-flat transmittance is observed for periods ranging from $P_y = 1826$ nm to $P_y = 1834$ nm. We also observe that the transmittance dip does not drop to zero, but reaches a level of 10% for $P_y = 1800$ nm.

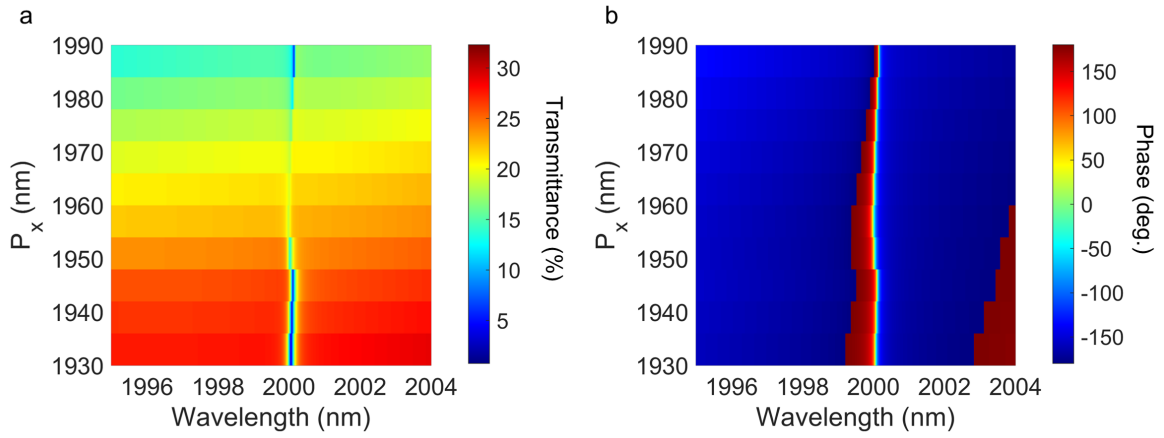


Figure S39: Transmittance **a** and phase of the transmitted light **b** as a function of the period in the x-direction P_x and wavelength. The geometrical parameters of the metasurface are the same as in Fig. 3f.

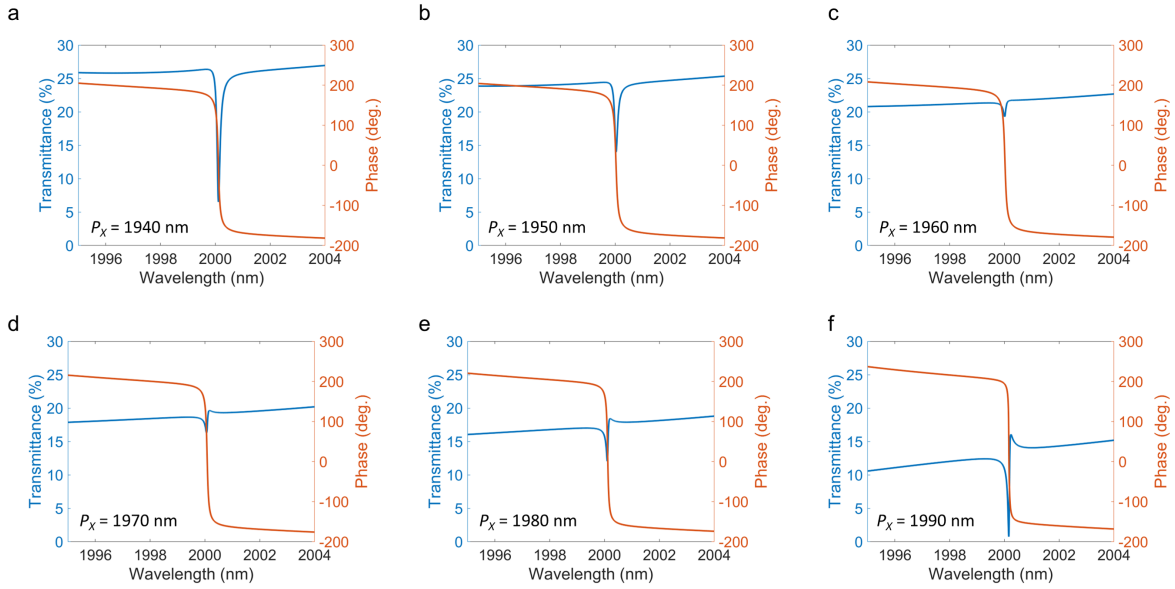


Figure S40: Transmittance and phase of the transmitted light as a function of wavelength for different values of the period in the x-direction P_x. The geometrical parameters are the same as in Fig. 3f. An almost-flat transmittance is observed for P_x ranging from 1960 nm to 1980 nm.

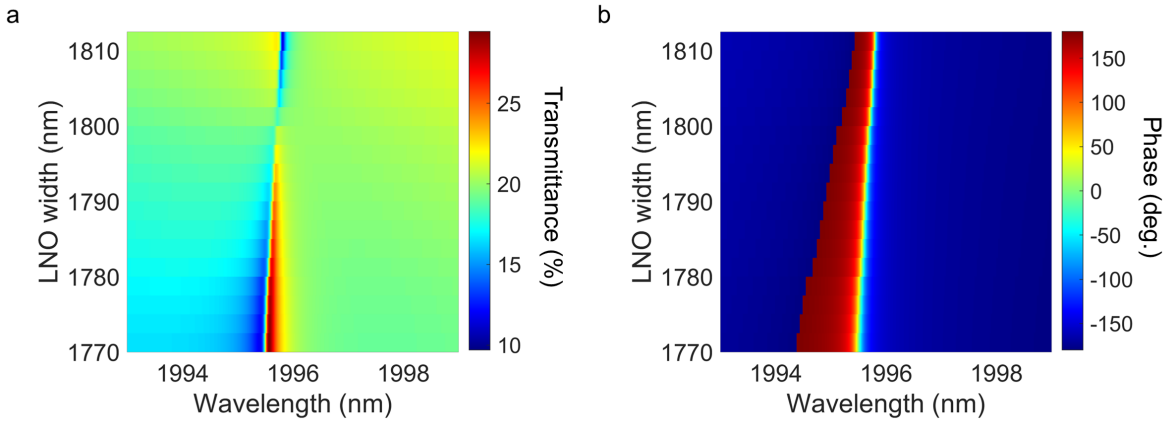


Figure S41: Transmittance **a** and phase of the transmitted light **b** as a function of the LN width w and wavelength. The geometrical parameters are the same as in Fig. 3f. To ensure the smoothness of the false-color plots, we introduced additional 20 nm × 20 nm × 20 nm mesh-override regions over the structure and simulation region. This additional mesh slightly affected the geometry sampling and the position of the resonance.

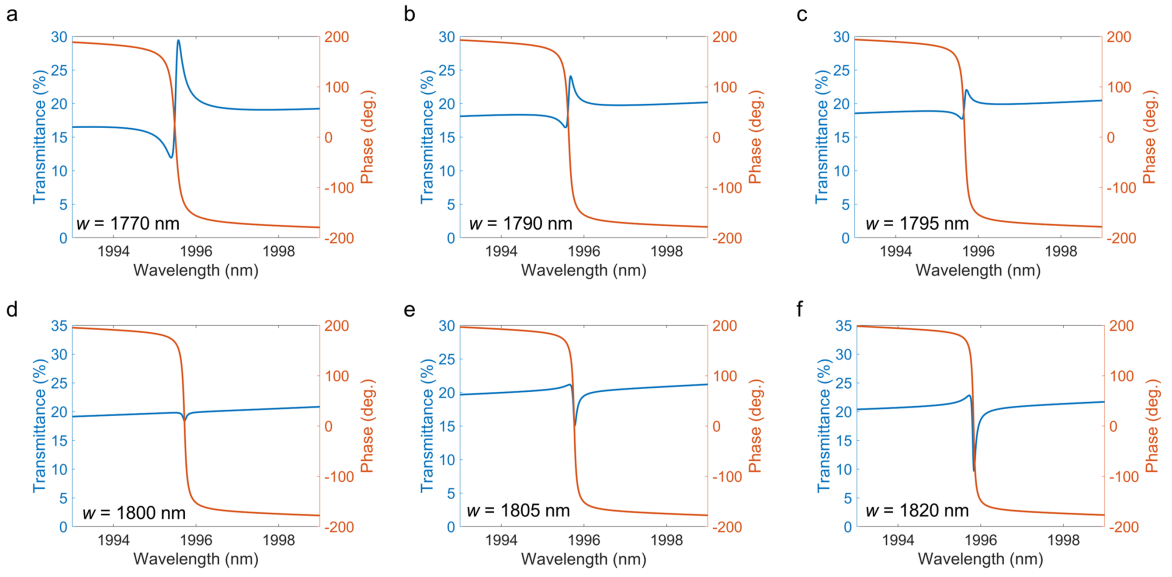


Figure S42: Transmittance and phase of the transmitted light as a function of wavelength for different values of the LN width w. The geometrical parameters are the same as in Fig. 3f. An almost-flat transmittance is observed at $w = 1800$ nm. However, the transmittance exhibits limited variation for widths ranging from 1790 nm to 1805 nm.

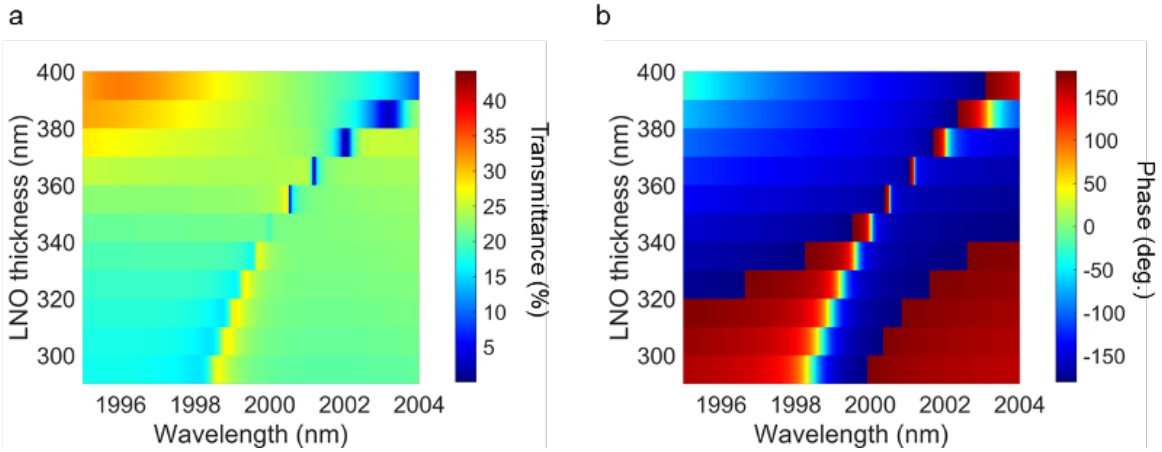


Figure S43: Transmittance **a** and phase of the transmitted light **b** as a function of the LN thickness t and wavelength. The geometrical parameters are the same as in Fig. 3f.

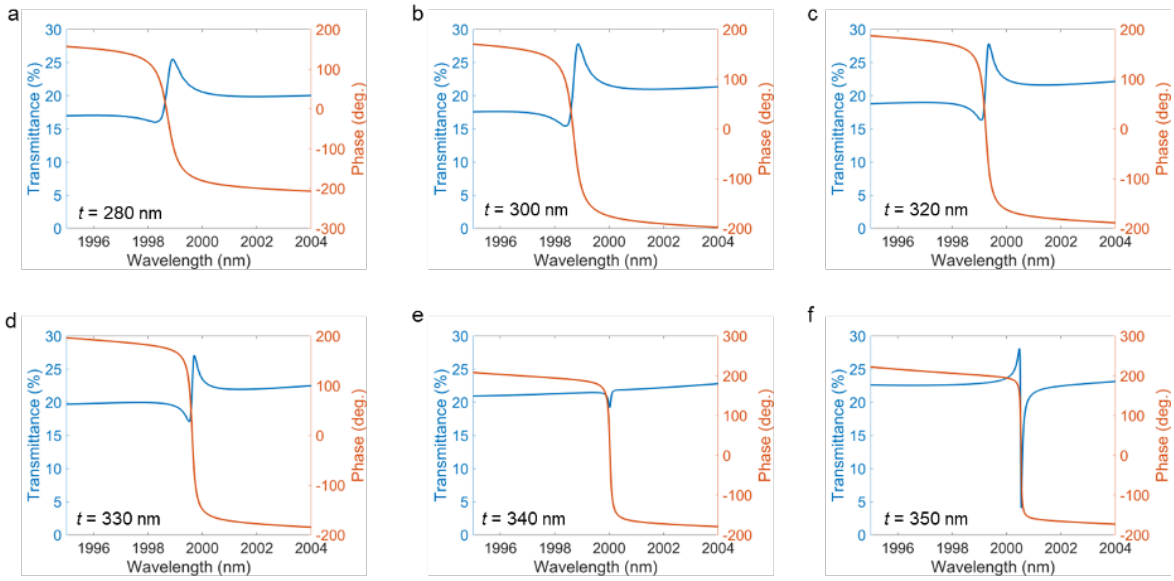


Figure S44: Transmittance and phase of the transmitted light as a function of wavelength for different LN thicknesses t. An almost-flat transmittance is observed at $t = 340$ nm, with limited variation for thicknesses ranging from 280 nm to 340 nm.

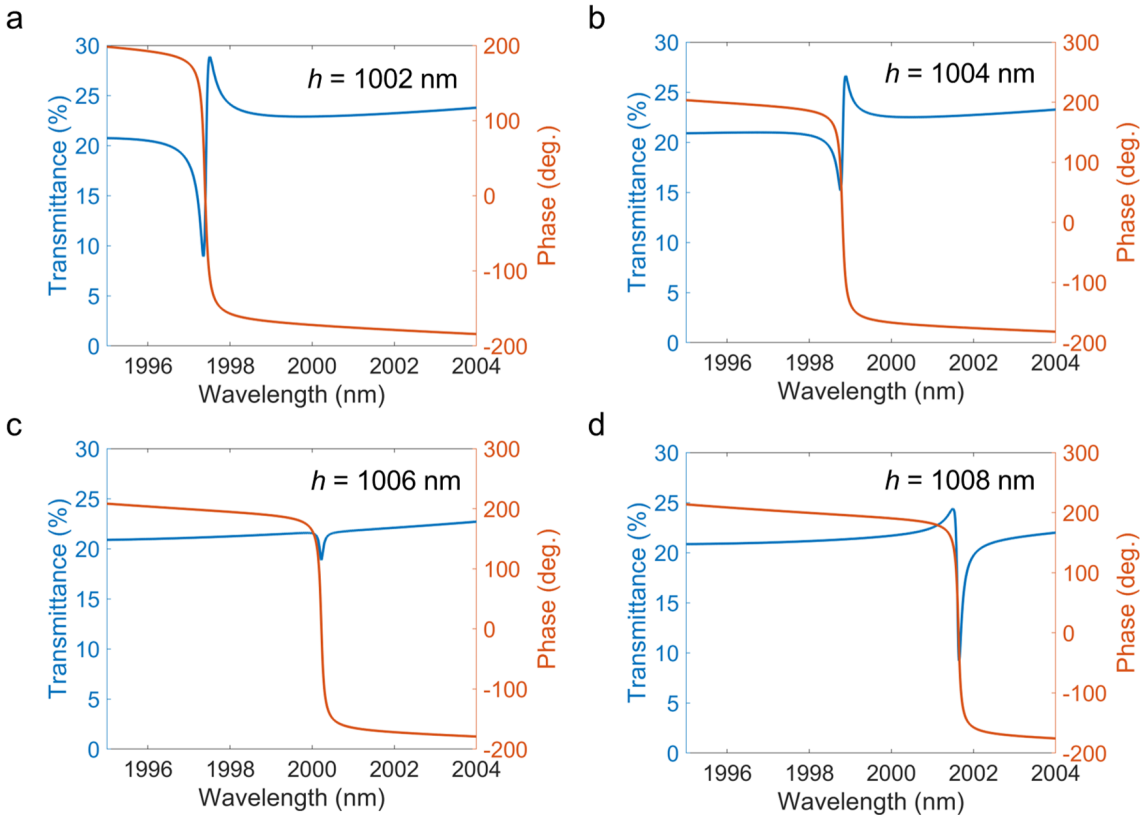


Figure S45: Transmittance and phase of the transmitted light as a function of wavelength for different values of the pillar height h. The geometrical parameters are the same as in Fig. 3f. An almost-flat transmittance is observed at $h = 1006$ nm, with limited variation for heights ranging from 1004 nm to 1006 nm.

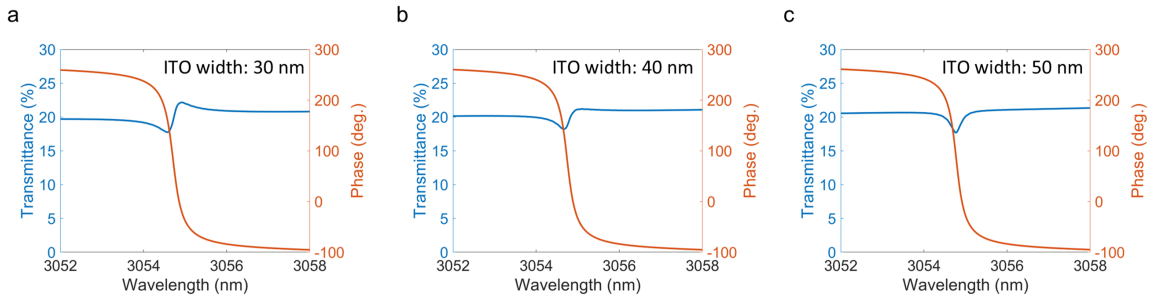


Figure S46: Transmittance and phase of the transmitted light as a function of wavelength for different values of the ITO electrode width. The geometrical parameters are the same as in Fig. 4b. A ± 10 nm modification of the ITO width leaves the resonance essentially flat.

References

[1] Shanhui Fan, Wonjoo Suh, and John D Joannopoulos. Temporal coupled-mode theory for the fano resonance in optical resonators. *Journal of the Optical Society of America A*, 20(3):569–572, 2003.

[2] Tong Wu and Philippe Lalanne. Exact maxwell evolution equation of resonator dynamics: Temporal coupled-mode theory revisited. *Optics Express*, 32(12):20904–20914, 2024.

[3] Hermann A Haus. *Waves and fields in optoelectronics*. Englewood Cliffs, NJ: Prentice-Hall, 1984.

[4] Rémi Colom, Elena Mikheeva, Karim Achouri, Jesus Zuniga-Perez, Nicolas Bonod, Olivier JF Martin, Sven Burger, and Patrice Genevet. Crossing of the branch cut: The topological origin of a universal 2π-phase retardation in non-hermitian metasurfaces. *Laser & Photonics Reviews*, 17 (6):2200976, 2023.

[5] Wei Liu and Yuri S Kivshar. Generalized kerker effects in nanophotonics and meta-optics. *Optics express*, 26(10):13085–13105, 2018.

[6] Yuhao Kang and Azriel Z Genack. Transmission zeros with topological symmetry in complex systems. *Physical Review B*, 103(10):L100201, 2021.

[7] Yariv Amnon and Pochi Yeh. *Photonics: Optical Electronics in Modern Communications*. Oxford University Press, 2007.

[8] Yao Ju, Hao Zhou, Ying Zhao, Fangjie Wang, Zuogang Yang, Xin Deng, Zhujing Wu, Deng Guoliang, and Haoyi Zuo. Hybrid resonance metasurface for a lithium niobate electro-optical modulator. *Optics Letters*, 47(22):5905–5908, 2022.

[9] David S. Kim, Hyunseok Kim, et al. Electrically programmable metasurface using edge-fed lateral biasing. *ACS Nano*, 14(5):6912–6920, 2020. doi: 10.1021/acsnano.0c02360.

[10] Emmanouel Hourdakis, Brian J Simonds, and Neil M Zimmerman. Submicron gap capacitor for measurement of breakdown voltage in air. *Review of scientific instruments*, 77(3), 2006.

[11] Haoxuan Wang, Russell S Brayfield, Amanda M Loveless, Adam M Darr, and Allen L Garner. Experimental study of gas breakdown and electron emission in nanoscale gaps at atmospheric pressure. *Applied Physics Letters*, 120(12), 2022.

[12] Justin Matthews. *The Experimental Study of Electrical Breakdowns in Vacuum Encapsulated MEMS Devices with Deep Submicron Capacitive Electrode Gaps.* Phd thesis, Georgia Institute of Technology, 2023.

[13] Yariv Amnon and Pochi Yeh. *Optical Waves in Crystals: Propagation and Control of Laser Radiation*. Wiley, 2003.

[14] M. Leidinger, A. Wiatrek, H. Hönig, P. Hönig, and B. Schmauss. High sensitivity optical characterization of lithium niobate in the mid-infrared. *Optics Express*, 23(17):21690–21703, 2015.

[15] Rei Kitamura, Laurent Pilon, and Miroslaw Jonasz. Optical constants of silica glass from extreme ultraviolet to far infrared at near room temperature. *Applied Optics*, 46(33):8118–8133, 2007.

[16] T. N. Nunley, S. M. Mansfield, and R. G. DeCorby. Optical constants of germanium thin films from 2 to 20 microns. *Journal of Vacuum Science & Technology B*, 34(6):061205, 2016.

[17] T. Amotchkina, M. Trubetskov, A. Tikhonravov, M. L. Grilli, G. B. Parravicini, and I. Krasilnikova. Optical constants of germanium thin films in the mid-infrared spectral range. *Applied Optics*, 59(5):A40–A46, 2020.

[18] D. Franta, I. Ohlídal, M. Špirková, and R. Král. Accurate optical constants of silicon in the infrared spectral region. *Thin Solid Films*, 541:12–16, 2013.

[19] Yao-Wei Huang, Wenhong T. Chen, Wei-Ting Chen, Pei-Cheng Wu, Ting-Chun Tsai, Meng-Tsun Tsai, Yun-Hsiang Chu, Eric J. Grubbs, Andrei A. Kanan, and Federico Capasso. Gate-tunable conducting oxide metasurfaces. *Nano Letters*, 16(9):5319–5325, 2016. doi: 10.1021/acs.nanolett.6b01754.